Correspondence to:
A. T. Tamoffo,
Alain.Tamoffo@hereon.de

Regionally Coupled Climate Model ROM Projects More Plausible Precipitation Change Over Central Equatorial Africa
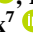
Alain T. Tamoffo[1] , **Torsten Weber**[1] , **Daniel Abel**[2] , **Katrin Ziegler**[2] , **William Cabos**[3] , **Dmitry V. Sein**[4,5,6] , **and Patrick Laux**[7]

[1]Climate Service Center Germany (GERICS), Helmholtz-Zentrum Hereon, Hamburg, Germany, [2]Institute of Geography and Geology, University of Wuerzburg, Wuerzburg, Germany, [3]Departamento de Física Y Matemáticas, Universidad de Alcalá, Alcalá de Henares, Spain, [4]Alfred Wegener Institute for Polar and Marine Research, Bremerhaven, Germany, [5]Shirshov Institute of Oceanology, Russian Academy of Science, Moscow, Russia, [6]Moscow Institute of Physics and Technology, Moscow, Russia, [7]Institute for Meteorology and Climate Research, Atmospheric Environmental Research, Karlsruhe Institute of Technology, Campus Alpine, Garmisch-Partenkirchen, Germany

Abstract Unraveling plausible future rainfall change (ΔPr) patterns is crucial for tailoring societies' responses to climate change-induced hazards. This study compares rainfall projections from the regionally coupled ocean model (ROM) and its atmospheric component, the regional atmospheric model REMO, over Central Equatorial Africa (CEA). Both models are forced by the Earth system model MPI-ESM-LR following the Representative Concentration Pathway 8.5. Results reveal increased rainfall across most of CEA, with ROM projecting more widespread and intensified wetting than REMO, although REMO produces more precipitation under future conditions, underscoring the influence of historical biases on REMO's projection. Examining processes underpinning changes unveils strong controls of sea and land surface temperature changes in ΔPr differences between the two models. Specifically, ROM mitigates warming more over the Atlantic than over CEA landmass compared to REMO, inducing enhancement of the Congo Basin cell and increased precipitable water content through specific humidity, affecting deep convection. Both models project enhanced Sahel and Kalahari thermal lows, with ROM better depicting the Kalahari low's warmer nature than the Sahel low. The resulting temperature gradients strengthen the northern and southern shallow meridional Hadley overturning circulation. ROM simulates the wetter conditions than REMO, attributed to its weaker northern Hadley Cell, which restricts the likelihood of northward moisture divergence toward the Sahel. Additionally, differences in mid-tropospheric moisture convergence differentiate between ROM and REMO's wetness relative to the historical period and under future conditions. ROM projections are more plausible, in association with the reliability of its added value under the historical climate and mechanisms underlying Δpr.

Plain Language Summary Discriminating models that project plausible rainfall change signals become increasingly necessary in a context where climate information surrounding future rainfall patterns is fraught with important uncertainties. It is not always straightforward to differentiate plausible projected changes from imperfect simulations as climate models are approximated solutions to mathematical and physical differential equations often solved with limited orders. One of the suggested approaches involves process-based assessments of projections. This approach requires that for example, rainfall change patterns must be underpinned by plausible mechanisms of change. A mechanism of change is plausible when it is identifiable in observational or reanalysis data sets. We applied such a method over Central Equatorial Africa using the regionally coupled ocean model (ROM) and its uncoupled version, the regional climate model REMO. The results show that projections based on ROM are more plausible thanks to a better depiction of the atmospheric baroclinicity associated with rainfall changes.

1. Introduction

The fitness of climate models for future projections relies on their representation of the relevant physical mechanisms' underpinning changes. This discriminatory criterion is currently very relevant due to the increasing availability of future climate data produced by various institutions or climate modeling groups. Climate change signals in precipitation vary from model to model and are sometimes contrasting (Dosio et al., 2021), highlighting uncertainties that may be broader than the change signal itself (Dosio et al., 2020; Pokam et al., 2018). This

Resources: Torsten Weber, William Cabos
Software: Alain T. Tamoffo, Torsten Weber, William Cabos, Dmitry V. Sein
Supervision: Torsten Weber, Daniel Abel, William Cabos, Dmitry V. Sein, Patrick Laux
Validation: Alain T. Tamoffo, Torsten Weber, Daniel Abel, Katrin Ziegler, Dmitry V. Sein, Patrick Laux
Visualization: Alain T. Tamoffo, Daniel Abel, Katrin Ziegler
Writing – original draft: Alain T. Tamoffo, Torsten Weber, Katrin Ziegler, William Cabos, Dmitry V. Sein
Writing – review & editing: Alain T. Tamoffo, Torsten Weber, Daniel Abel, Katrin Ziegler, William Cabos, Dmitry V. Sein, Patrick Laux

assertion holds particular relevance over regions such as Central Equatorial Africa (CEA), where climate models are less constrained by observational records and exhibit large differences in their climatology (Washington et al., 2013). The sources of uncertainty in models' projections are diverse. They may encompass aspects such as the structure of Earth system models (ESMs) or regional climate models (RCMs), future greenhouse gas emissions, models' parameterization, internal variability of the climate system, and the configuration of the models, including their coupling with other Earth system components (Kay et al., 2008; Kirtman et al., 2013; Laux et al., 2021; Zhou et al., 2020). Distinguishing models that project plausible future changes is therefore crucial to support decision-makers in tailoring efficient disaster preparedness, adaptation planning, and mitigation strategies (Laux et al., 2021). To some extent, the survival of the forest ecosystem in the Congo Basin (Vizy et al., 2023) relies on the reliability of climate information needed for informing societal responses.

Many studies have addressed the question of how to discriminate between plausible climate change signals simulated by models. In this regard, they have proposed process-oriented analysis protocols (e.g., James et al., 2015, 2018; Neelin et al., 2023). In advance, it's not evident that a model simulates the exact observed climatology, especially in terms of magnitude. This is especially true since the output variables of a model are mostly approximate solutions to mathematical and physical differential equations. However, at the very least, one should demand that a model represents the climatology of a region in accordance with the physical processes underlying the (regional) climate system. This requirement helps in eliminating RCMs that add value for the wrong reasons, that is, improvements in rainfall climatology are not associated with enhancements in underlying mechanisms (Tamoffo et al., 2020). Such models would lack sensitivity to external forcings and, therefore, would not be appropriate to project future climates, where high sensitivity is needed to detect signals of climate change related to anthropogenic forcings (Rowell et al., 2015). A model that accurately simulates a credible historical rainfall system (i.e., where modelled underlying rainfall climatology's drivers are also present in reanalysis or observational data) is more likely to simulate a plausible future rainfall system (James et al., 2015; King et al., 2020). Afterward, investigating the physical processes' underpinning changes helps shed light on the plausibility of projections. A plausible rainfall change pattern is driven by plausible mechanisms (i.e., processes underlying rainfall change can be identified in reanalysis or observational data). When the mechanisms driving rainfall changes are different from those governing the observed climatology, this casts doubt on projections.

Few studies have attempted to differentiate between plausible and implausible future projections over equatorial Africa, with most focusing on stand-alone atmospheric RCMs (e.g., James et al., 2015; Tamoffo, Akinsanola, & Weber, 2023) and ESMs from various phases of the Coupled Model Intercomparison Project (CMIP; Creese, Washington, & Jones, 2019; Creese, Washington, & Munday, 2019; James et al., 2015; Monerie et al., 2016, 2020). For instance, the process-based analysis helped discredit the drying trend signal as modelled by RCMs and GCMs over West Africa (James et al., 2015). The projected changes in the atmospheric circulation associated with the drying trend were not present in reanalyses. Similarly, over the eastern Congo Basin, the projected drier conditions by historically dry CMIP5 models were found doubtful due to the misrepresentation of the northern component of the African Easterly Jet (AEJ) during the historical period, resulting in projections of a different wetting pattern (Creese, Washington, & Munday, 2019). Tamoffo, Akinsanola, and Weber (2023) also reported doubtful West African monsoon rainfall change-related shift in AEJ, linked to a misrepresentation of the baseline structure of the vertical profile of the zonal circulation simulated by the regional model version 4 (RegCM4). Given the wide spectrum of physical processes sustaining CEA's rainfall system, numerous other mechanisms can aid in diagnosing the plausibility of projections, as presented in Section 2.

As aforementioned, uncertainties in a region's projections can also arise from the way models are configured to simulate the climate system. Notably, some studies showed that regional climate systems with strong air-sea interactions are better represented by Regional Earth System Models (RESMs), that is, RCMs coupled with, for instance, an ocean model, than their stand-alone atmospheric counterpart (Paxian et al., 2016; Ratnam et al., 2015; Sein et al., 2015; Zou & Zhou, 2016). In this perspective, a preliminary study by Weber et al. (2022) revealed that coupling the atmosphere-only RCM REMO with the global Max Planck Institute for Meteorology Ocean Model (MPIOM) leads to improvements in the representativeness of precipitation over Sub-Saharan Africa regions. Additionally, the resulting regionally coupled ocean-atmosphere model (Regional Ocean Model, ROM) also modifies climate change signals in rainfall indices, including strengthening, weakening, or even sign reversal. Tamoffo, Weber, Cabos, Sein, et al. (2024) recently scrutinized the plausibility of the ROM's added value compared to REMO over CEA during the September-November (SON) rainiest season. They found that ROM improves the precipitation climatology for the right reasons: indeed, the explicit representation of the

ocean results in a substantial reduction of warm sea surface temperature (SST) biases often simulated by CMIP models over the eastern equatorial Atlantic Ocean (Creese & Washington, 2018). Subsequently, improvements in SSTs lead to enhancements in air-sea interactions through better representations of surface thermal and pressure gradients. In response, the representation of the regional atmospheric circulation is ameliorated, and thus, the associated rainfall climatology improves.

The present study aims to complement the former study by Tamoffo, Weber, Cabos, Sein, et al. (2024) in examining the plausibility of projections as simulated by ROM compared to REMO. The main objective of this study is to determine which of the two models (REMO vs. ROM) projects the most plausible changes in precipitation over CEA. We assume that whether the global ocean model MPIOM simulates more realistic SSTs in ROM than the prescribed SSTs from the driving ESM in REMO under historical climate conditions, a similar situation may be evident in future projections. Therefore, under a future climate with increased warming, we hypothesize that the coupled model ROM may better simulate atmospheric baroclinicity than the uncoupled model REMO, leading to a more confident representation of rainfall changes. As mentioned above, the reliability of each model's rainfall changes will be deduced from its ability to simulate the major physical mechanisms underlying these changes.

The remainder of the paper is structured as follows: Data and metrics used to diagnose mechanisms are described in Section 2 and changes in the CEA rainfall in ROM and REMO models are presented in Section 3. Physical processes and underlying mechanisms associated with rainfall changes are shown in Sections 4 and 5 discusses and summarizes the document.

2. Data and Methods

2.1. Data

The simulation data used in this study are products of the regionally coupled ocean-atmosphere model ROM (Sein et al., 2015) and its uncoupled counterpart REMO (Jacob, 2001; Jacob et al., 2001), which is similar to its 2015 version (REMO2015; Jacob et al., 2012). The regionally coupled model ROM consists of a global ocean–sea ice model (MPIOM; Jungclaus et al., 2013) coupled with a regional atmospheric model (REMO) and a global terrestrial hydrology model (HD). REMO, the atmospheric component of ROM, is a regional model with a dynamical core based on the Europa-Model of the German Weather Service (Majewski, 1991), and its physical parameterizations are derived from the global climate model ECHAM (Roeckner et al., 1996, 2003). For this study, the REMO domain includes Africa, parts of the Indian Ocean, and the Mediterranean region, with a resolution of 25 km. The MPIOM configuration used in this version of ROM places the grid poles over North America and northwestern Africa. Its horizontal resolution reaches approximately 10 km near western Africa and is gradually decreasing to 100 km in the southern oceans. The model includes 40 *vertical levels*, with thickness increasing toward the ocean floor. The global MPIOM domain is divided into a coupled subdomain, where the ocean and atmosphere interact, and an uncoupled region where the ocean model is driven by the Max Planck Institute Earth System Model lower resolution (MPI-ESM-LR; Giorgetta et al., 2013) atmospheric data without feedback (see Figure 1). This configuration allows for high model resolution in the coupled subdomain in a computationally efficient manner. The coupling interval between the ocean and atmosphere is 3 hr. Lateral atmospheric and upper ocean boundary conditions outside the coupled domain are also provided by the global driving model. We explored the sensitivity of the model results to changes in the parameterization of large-scale precipitation. Since the results of these sensitivity experiments do not alter our main conclusions, we do not present them here.

For initialization, the ocean model underwent a two-cycle spin-up, forced by the 1958–2002 ERA-Interim data, totaling 90 years. At the start of the spin-up, the ocean was at rest, with its temperature and salinity initialized from the Levitus January climatology. Over these 90 years, the ocean velocities, salinity, and temperature in MPIOM adjusted, reaching a state of quasi-equilibrium, particularly in the upper ocean layers. The subsequent spin-up of the coupled reanalysis- and ESM-forced runs continued from the final state of the forced MPIOM run. The ESM-forced experiment setup then underwent further spin-up using MPI-ESM-LR forcing data starting from 1950. Meanwhile, the reanalysis-forced simulation was forced by reanalysis data from ERA40 (1958–1980) and ERA-Interim (1981–2002).
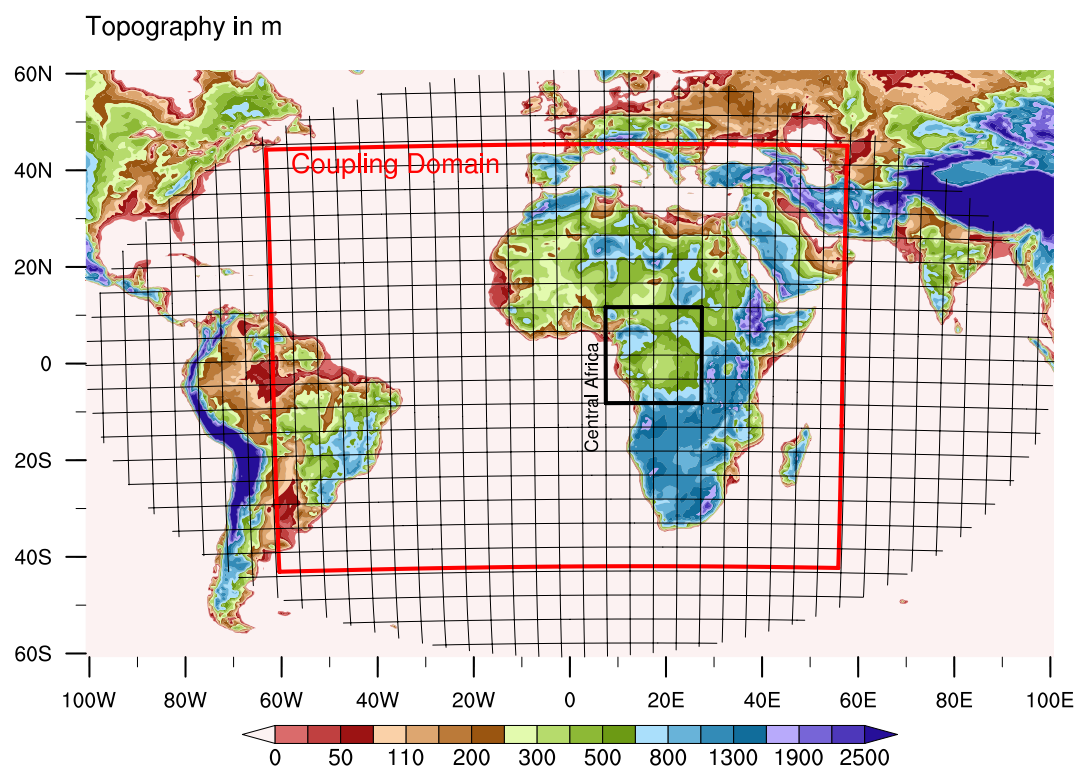
Figure 1. The coupling area (red box) is displayed along with the topography of the domain (m) from NASA GTOPO30. Also shown is the Central Africa region (black box).

During the coupled spin-up, special attention was given to the prolonged thermohaline and dynamical adjustments, particularly in the deeper ocean layers. The reanalysis-forced run underwent its spin-up first with ERA-Interim, followed by ERA40, as the warming trend observed during the 1981–2002 run made it unsuitable as the initial state for the production run. Instead, the ROM-reanalysis production run commenced from a state closer to observed conditions. The impact of forcing changes was considered insignificant after 1 or 2 years, particularly in SSTs. Therefore, the production run for both setups commenced when the initial state reached quasi-equilibrium, with ROM-reanalysis simulation starting from a realistic initial state, despite limitations in discarding the initial years.

As demonstrated by Paxian et al. (2016) in the context of decadal predictions, and by Sein et al. (2015), Cabos et al. (2017), Tamoffo, Weber, Cabos, Sein, et al. (2024), and Tamoffo, Weber, Cabos, Monerie, et al. (2024) for historical simulations, the Atlantic SST bias is significantly reduced in coupled regional simulations. This reduction is attributed to the representation of fine-scale air-sea interactions at high atmospheric and oceanic resolutions, which improve the deficient winds in GCMs, enhance surface ocean currents, intensify the cold water upwelling of the Benguela Current, and reduce the southward extension of the warm Angola Current. Consequently, the simulated ITCZ remains in its observed position over the northern Guinea Coast.

The primary distinction between REMO and ROM lies in the source of SSTs. In REMO simulations, SSTs are prescribed by MPI-ESM-LR, while in ROM, SSTs are generated by the oceanic component of the global ocean model MPIOM. REMO is thus influenced by biased SSTs inherited from the driving ESM MPI-ESM-LR, whereas ROM has the potential to simulate SSTs more accurately than MPI-ESM-LR, particularly in regions distant from the boundaries of the coupling domain (Sein et al., 2014), such as CEA. An important consequence is the expectation of changes in surface heat and momentum fluxes between ROM and REMO (Cabos et al., 2020), potentially leading to modifications in low-level cloud fraction through alterations in the boundary layer turbulent mixing (Sherwood et al., 2014; Vial et al., 2016). The choice of the driving ESM is motivated by the consistencies between the downscaling tool and the forcing fields. Indeed, ROM and MPI-ESM-LR share the same ocean component, which is MPIOM. Similarly, REMO and ROM are both based on the same physical parameterizations and dynamical core as ECHAM, the latter being the atmospheric component of MPI-ESM-LR (Jacob et al., 2012).

Historical simulations span from 1950 to 2005 and are based on observed natural and anthropogenic greenhouse gas (GHG) concentrations. Projections extend from 2050 to 2099 and are influenced by the high-emission Representative Concentration Pathway 8.5 (RCP8.5; van Vuuren et al., 2011). RCP8.5 corresponds to CO_2 equivalent emissions of around >1,370 ppm at the end of the century. Although the sixth assessment report (AR6) of the Intergovernmental Panel on Climate Change (IPCC) may consider the likelihood of RCP8.5 as "low" (but not ruled out; Lee et al., 2021), we chose to focus our analysis on RCP8.5. This choice allows us to maximize the projected precipitation changes, which, at lower emission scenarios, may be masked by internal variability (e.g., Doblas-Reyes et al., 2021).

2.2. Methods

We start our analyses by characterizing rainfall change patterns (ΔPr) as simulated by each model between the late twentieth and late twenty-first century over CEA (defined as 10°S–10°N; 10°–30°E, see black box in Figure 1). In doing so, we also examined the spatiotemporal changes in the mean seasonal position of the rain-band. This helps elucidate whether ΔPr patterns simulated by each model are associated with a shift in the location of the rain-band due to global warming (indicating a prevalence of dynamic factors driving changes) or, alternatively, if the ΔPr patterns are primarily linked to changes in precipitation magnitude. The latter scenario suggests a dominance of thermodynamic factors driving changes (Monerie et al., 2020). The zonal mean position of the rain-band is determined using the barycentre theorem, as defined in d'Orgeval (2008), as follows:

$$G(t) = \frac{\sum_{i=1}^{n} y_i P_i}{\sum_{i=1}^{n} P_i} \tag{1}$$

where P_i is precipitation at latitude y_i. The barycentre G is computed for each time step t.

The analysis of the Probability Density Functions (PDFs) helps to elucidate whether warming does not alter the monthly precipitation characteristics over the late 21st century. For this purpose, we utilized the Gamma distribution (Band et al., 2022; Lloyd-Hughes & Saunders, 2002) following the expression in Equation 2:

$$f(P_i) = \frac{1}{\beta^{\alpha}\Gamma(\alpha)} P_i^{\alpha-1} e^{-P_i/\beta} \text{ for } P_i > 0 \tag{2}$$

where $\alpha > 0$ is the shape parameter, $\beta > 0$ is the scale parameter, $P_i > 0$ is the rainfall amount, and $\Gamma(\alpha)$ the Gamma function. PDFs based on observational data from CHIRPS2 (Funk et al., 2015), GPCC.v2020 (Schneider et al., 2022), CRU.ts4.05 (Harris et al., 2020), and from the reanalysis ERA5 (Hersbach et al., 2020) are also included in the analysis to gain insight into which model projects a plausible distributed rainfall pattern.

Afterward, processes associated with ΔPr patterns are diagnosed. We first look at both REMO and ROM projected changes in SSTs (ΔSST) and surface temperatures (ΔTs) on the one hand, and then changes in sea level pressure (ΔSLP) and surface pressure (ΔSP) on the other. Changes in $SSTs$ and Ts can potentially impact the regional hydrological cycle, either enhancing or weakening it (Seager et al., 2010; Seneviratne et al., 2010). Additionally, alterations in $SSTs$, Ts, SLP, and SP influence zonal and meridional circulation by modifying surface thermal and pressure contrasts and gradients. Therefore, we compute the land-ocean thermal (∇T) and pressure (∇P) contrasts for both historical and future periods for each model. Thermal and pressure contrasts are respectively calculated as the differences between land Ts and ocean $SSTs$, and land surface pressure (SP) and ocean sea level pressure (SLP). These differences are computed between the interior of the continent (15°–30°E; 10°S–5°N) and the eastern Atlantic Ocean (0°–10°E; 0–10°S). The pair (∇T, ∇P) serves as a precursor to a zonal shallow overturning and counterclockwise circulation over the Congo Basin, known as the Congo Basin cell (Longandjo & Rouault, 2020). In turn, the Congo Basin cell influences the precipitable water, regulating deep convection (Longandjo & Rouault, 2023). We therefore investigated changes in the Congo Basin cell as projected by each model. For this purpose, the water vapor mass transported within the mean zonal circulation is estimated using the zonal mass-weighted stream functions (Ψz; e.g., Stachnik & Schumacher, 2011), following the equation:

$$\Psi Z(p) = \frac{2\pi R}{g} \int_{sp}^{P} [u]\, dp \tag{3}$$

where R is the Earth's radius [m], g is the constant of gravity, SP the surface pressure, $P \in [1{,}000, 500\ \text{hPa}]$, and the operator $[u]$ symbolizes the meridional average of the zonal wind. The Congo Basin cell is delineated by the contour $\Psi Z = 0$, indicating the commencement of negative stream functions ($\Psi Z < 0$) characteristic of the cell. Considering that the surface meridional temperature gradient forces the middle-level circulation over CEA (Kuete et al., 2019), we also examine how this gradient will respond to the warming as simulated by each model. Subsequently, changes in middle-level circulation are explored through the AEJ. Here, we focus on the mean intensity and latitudinal migration of the jet's northern (AEJ-N) and southern (AEJ-S) components. The features of the jet are well-known, as described by Nicholson and Grist (2003) and Kuete et al. (2019). Broadly, AEJs are defined as mid-tropospheric (700–600 hPa) easterly winds with a speed exceeding 6 m/s. The AEJ-N component lies within latitudes 0°–15°N and is active all year round, while the AEJ-S component lies within latitudes 0°–10°S and is active only during SON.

Previous studies (e.g., Jackson et al., 2009) posited that SON is the rainiest season over CEA due to the activation of both AEJ-N and AEJ-S branches during this time of year, which intensifies mass convergence in the middle layers, increasing the number of mesoscale convective systems (MCSs). A recent work by Longandjo and Rouault (2023), instead, showed that over Central Africa, a shallow meridional overturning circulation determines rainfall seasonality. These authors found that shallow and deep Hadley cells coexist within the region throughout the year. While the deep cell serves as an engine of energy transport from the equator toward the poles, the shallow cell features a shallow meridional circulation, with its moisture transport disappearing and converging in the mid-troposphere rather than at the lower troposphere. They reported a weak contribution of moisture convergence emanating from AEJs. To ascertain whether such a process plays a role in shaping ΔPr patterns, we diagnose changes in the meridional circulation using meridional mass-weighted stream functions, as described by the following equation (Stachnik & Schumacher, 2011):

$$\Psi M(p) = \frac{2\pi R \cos(\phi)}{g} \int_{sp}^{P} [v]\, dp \tag{4}$$

where ϕ denotes latitudes, $P \in [1{,}000, 100\ \text{hPa}]$, while the operator $[v]$ symbolizes a zonal average of the meridional wind.

It is established that the seasonal cycle of rainfall correlates with that of moisture flux convergence $[\nabla \cdot (qV)]$ over CEA (Pokam et al., 2012). Similarly, the seasonal cycle of $\nabla \cdot (qV)$ mirrors that of the shallow meridional circulation (Longandjo & Rouault, 2023). Consequently, a plausible ΔPr pattern is essentially conditioned by a plausible change in $\nabla \cdot (qV)$. In a given region, $\nabla \cdot (qV)$ can be split into two terms: the moisture advection term ($V\nabla \cdot q$) and the moisture convergence term ($q\nabla \cdot V$) so that:

$$\nabla \cdot (qV) = V\nabla \cdot q + q\nabla \cdot V \tag{5}$$

Consistently, Cook and Vizy (2021) and Longandjo and Rouault (2023) showed that the second term on the right side of Equation 5 ($q\nabla \cdot V$) prevails in $\nabla \cdot (qV)$ over CEA and is responsible for uplift from the mid-troposphere rather than from lower layers. We hypothesize that changes in $q\nabla \cdot V$ should also prevail over changes in $V\nabla \cdot q$, contributing to the overall changes in $\nabla \cdot (qV)$.

The climate change signal (hereafter Δ) in atmospheric fields is estimated following the equation: $\Delta = (.)_{\text{future}} - (.)_{\text{historical}}$ where the historical period spans from 1971 to 2000 for the late twentieth century, and the future covers the period from 2070 to 2099 for the late twenty-first century.
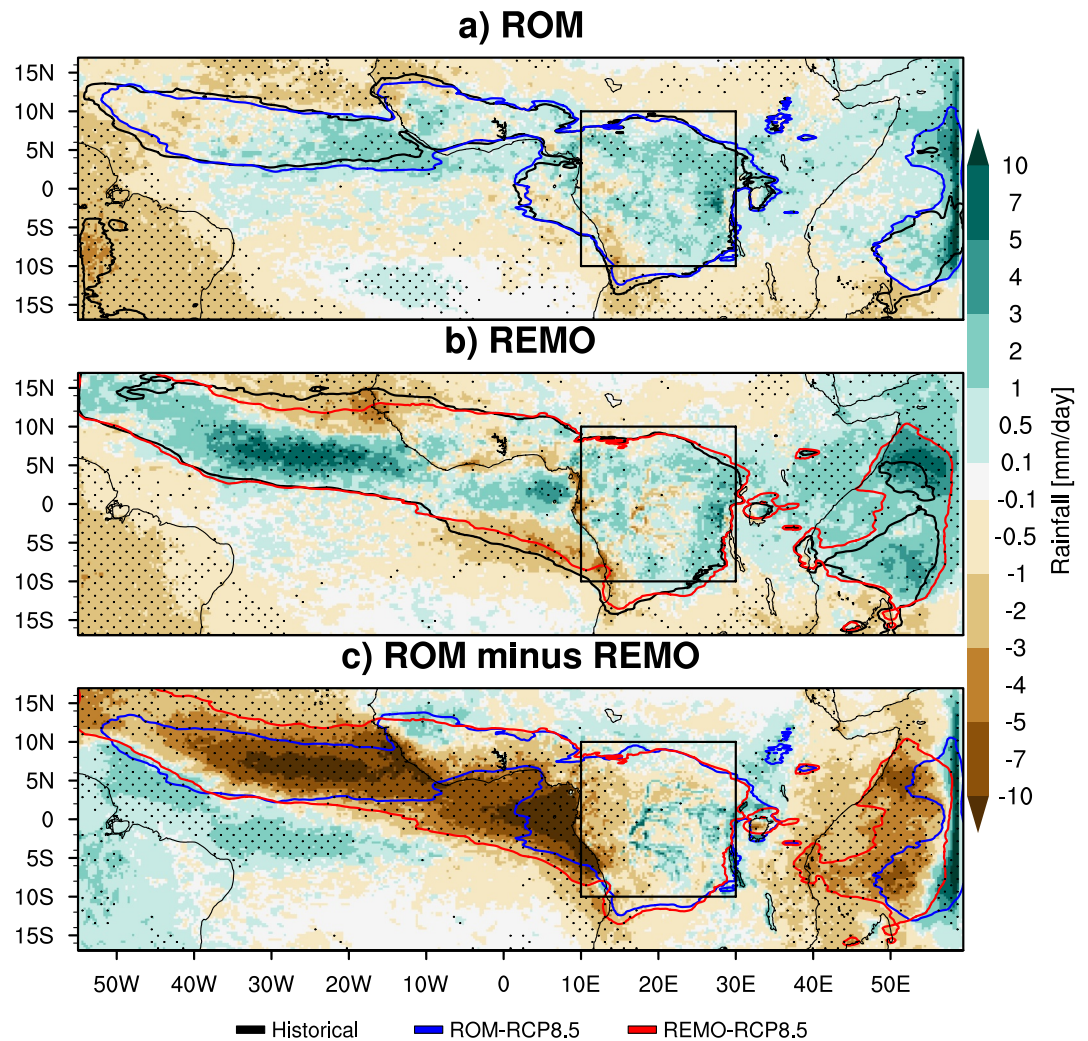
Figure 2. Future (2070–2099) minus historical (1971–2000) mean SON seasonal rainfall changes (ΔPr, in mm/day), for (a) **ROM** and (b) **REMO**. Panel (c) displays the difference **ROM minus REMO** under the future period (2070–2099). Contours indicate the extent of the rain-band (i.e., precipitation larger than 3 mm/day) under the historical (black) and future (blue and red). The stippling highlights the grid points where the difference future (2070–2099) minus historical (1971–2000) of the data set under consideration (a and b) or the ROM minus REMO difference (c) is statistically significant at 95% confidence level using the Student's t-test. The black box denotes CEA.

3. REMO Versus ROM: Rainfall Changes

Figure 2 illustrates the spatial pattern of projected rainfall changes (ΔPr) as simulated by ROM (Figure 2a) and REMO (Figure 2b). Additionally, the difference (ROM minus REMO) in future conditions is also presented in Figure 2c to provide insight into the effect of the coupling under enhanced global warming conditions, regardless of historical conditions. Consistently, both ROM and REMO indicate that most areas over CEA will moisten ($\Delta Pr > 0$; 72% and 66% of the total CEA's area, respectively). However, there are exceptions, with a few grid points over the West and South West in ROM, over the coastline and in the core of the Congo Basin in REMO, where drier conditions ($\Delta Pr < 0$) are expected (27% and 33% of the total CEA's area, respectively). In terms of magnitude (Figure S1 in Supporting Information S1), ROM simulates an enhanced mean regional rainfall change of +0.59 mm/day while REMO simulates about half, that is, +0.30 mm/day. Therefore, ROM projects more regionally widespread and stronger wetting in the future than REMO. Furthermore, the coupled model ROM simulates a more pronounced increase in future precipitation compared to its historical period than the uncoupled model REMO. However, REMO shows a higher future precipitation amount than ROM. Notably, REMO's historical rainfall is closely aligned with its projection. This suggests that the historical rainfall bias in REMO, as
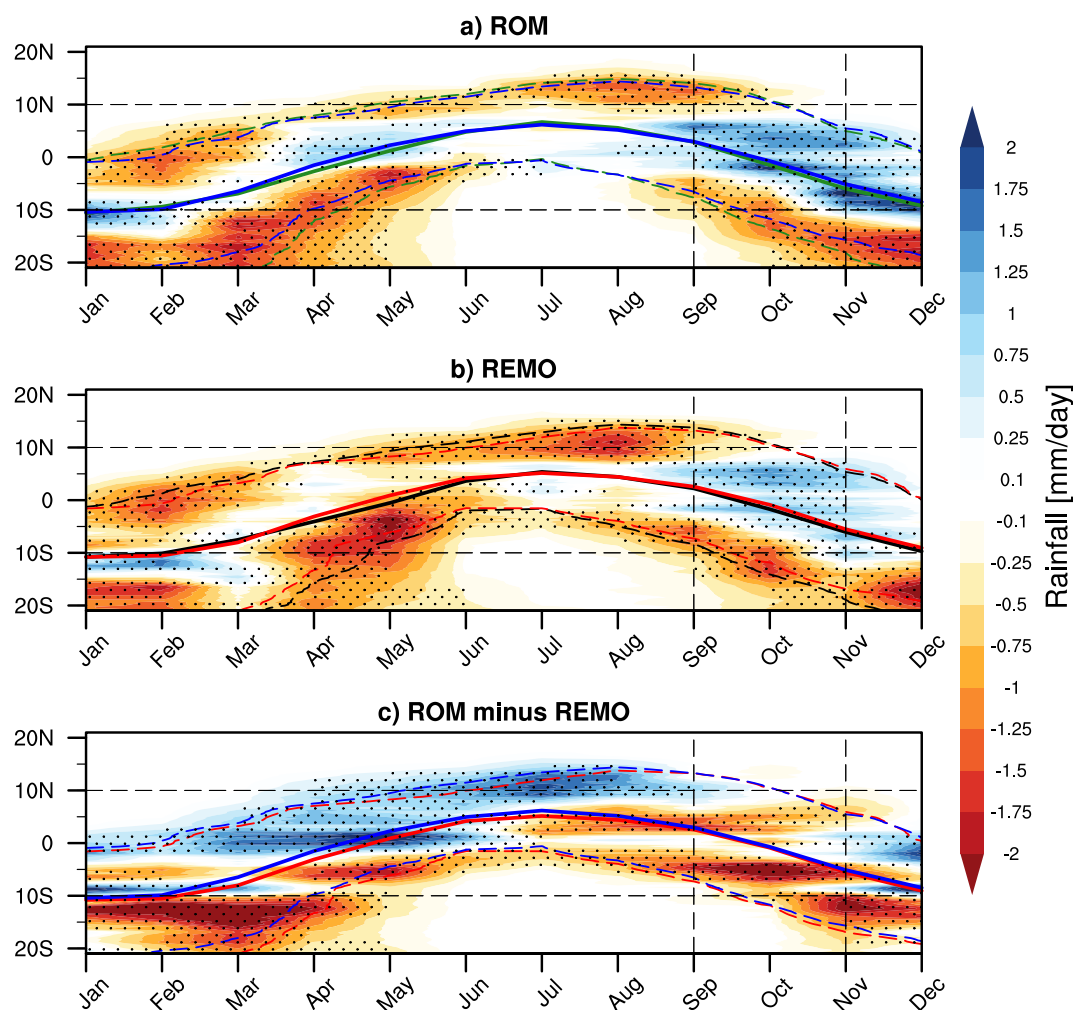
Figure 3. Latitude-time cross sections of the future (2070–2099) minus historical (1971–2000) annual cycle of rainfall changes (ΔPr, in mm/day), for (a) **ROM** and (b) **REMO**. Panel (c) displays the difference **ROM minus REMO** under the future period (2070–2099). Dashed line contours indicate the extent of the rain-band (i.e., precipitation larger than 3 mm/day) under the historical (forestgreen for (a) ROM and black for (b) REMO) and future (blue for (a) ROM and red for (b) REMO). The solid contours denote the mean monthly rain-band locations under the historical (forestgreen for (a) ROM and black for (b) REMO) and future (blue for (a) ROM and red for (b) REMO). The stippling highlights the grid points where the difference future (2070–2099) minus historical (1971–2000) of the data set under consideration (a-(b) or the ROM minus REMO difference (c) is statistically significant at 95% confidence level using the Student's t-test. The horizontal dashed bars limit CEA's latitudes while vertical dashed bars denote the SON season.

demonstrated in Tamoffo, Weber, Cabos, Sein, et al. (2024), significantly influences its projected climate change signal. This result is substantiated by the fact that, although the precipitation increase of ROM is stronger over time than in REMO, the coupled version projects lower rainfall amounts under future conditions than the uncoupled one (Figure 2c and Figure S1 in Supporting Information S1).

We further examined intraseasonal ΔPr patterns, as depicted in Figure 3. A prevailing drying, not anticipated from Figure 2, is highlighted throughout the southern side of the rain-band during SON, consistently simulated by both ROM (Figure 3a) and REMO (Figure 3b). This drying is associated with a northward shift of the southern side of the rain-band. On the northern side, both models indicate that the rain-band edge is simulated to be south of its historical position, leading to drying in September. The reverse situation is expected in November, leading to wetting, while no substantial change is projected in October, in association with consistencies between historical and future rain-band positions. This suggests a narrowing of the rain-band, potentially leading to consequences such as the shrinking of the Congo rainforest and, consequently, the southward expansion of Sahelian conditions (Thomas & Nigam, 2018; Vizy et al., 2023). Both ROM and REMO exhibit superposed historical and future mean
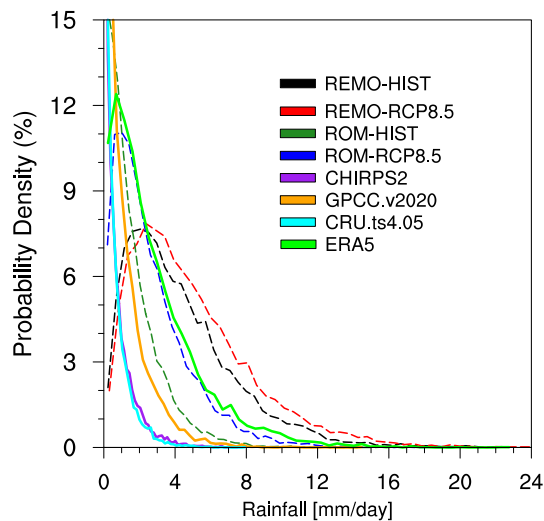
Figure 4. Probability Density Functions (PDFs) of monthly precipitation (mm/day) from observations (solid lines) CRU.ts4.05 (cyan), GPCC.v2020 (orange) and CHIRPS2 (purple), reanalysis ERA5 (green) as well as from REMO and ROM runs (dashed lines) under the historical period (black and dark-green, respectively) and future period (red and blue, respectively). Historical simulations cover 1971–2000 and the future 2070–2099. Observations and the reanalysis ERA5 are used from 1980 to 2000 except CHIRPS2 which covers the period 1981–2000.

monthly rain-band positions (the barycentre). Similarly, the two models display superposed future mean monthly rain-band positions.

Based on the aforementioned results, the following stepwise conclusions can be drawn: (a) the north-south shifts, albeit slight, in the northern and southern edges' positions of the rain-band between the historical and future periods as simulated by the two models presage an influence of dynamic processes on the ΔPr patterns. (b) However, both models concur that the monthly mean positions of the rain-band (barycentre) will not undergo substantial changes between the historical and future periods, arguing for a modulating effect of thermodynamic processes. Therefore, both dynamic and thermodynamic processes would co-contribute to shaping ΔPr patterns, which aligns with previous work by Creese, Washington, and Jones (2019) and Tamoffo, Dosio, et al. (2023). Notably, the second stepwise conclusion suggests a prevalence of thermodynamics over dynamic drivers.

Figure 4 displays the PDFs of CEA's precipitation from both ROM and REMO models under both historical and future periods. At first sight, the two models simulate similar distributions between the historical and future periods. However, REMO generally exhibits wider distributions and lower peaks than ROM under both periods indicating more heavy precipitation events. This aligns with the general tendency of CORDEX-CORE RCM to overestimate precipitation during SON in Central Africa (Bangelesa et al., 2023). ROM and REMO show an enhanced distribution under global warming, but the shapes of distributions based on ROM are closer to those of observations than those based on REMO. Specifically, ROM's distribution during the historical climate closely matches observations, while its projection aligns with ERA5. The change over time, thus, lies within the range of observational or reanalysis data sets' uncertainty. Conversely, REMO consistently features different distributions compared to both observations and the reanalysis over the two periods.

We previously noted that the model's historical rainfall bias strongly influences its ΔPr patterns. Indeed, REMO, which historically experiences more rainfall than ROM, continues to do so in the future, but contrastingly, ROM expects a stronger mean regional ΔPr than REMO (Figure S1 in Supporting Information S1). There is also a strong relationship between the historical and future annual precipitation cycles as modeled by the two RCMs, with ROM featuring a correlation of $r = 0.97$ and REMO exhibiting $r = 0.98$ (Figure S2a in Supporting Information S1). Similarly, ROM strongly correlates with REMO in the historical and future annual cycles (Figure S2b in Supporting Information S1). This suggests that the changes induced by warming have not disrupted the seasonality of precipitation; instead, they may have amplified or attenuated its magnitude. A direct consequence is that the physical processes underpinning ΔPr patterns may then be investigated within the large spectrum of mechanisms underlying historical climatology. Additionally, the fact that ROM adds value over REMO in historical climatology (Tamoffo, Weber, Cabos, Sein, et al., 2024) advocates, hypothetically, the reliability of its ΔPr pattern. To shed light on which model projects a plausible ΔPr pattern, we examine the drivers of rainfall changes in the next section.

4. Mechanisms of Rainfall Changes

It is worth noting that a thorough process-based evaluation of the added value resulting from both models has been conducted in a previous study by Tamoffo, Weber, Cabos, Sein et al. (2024), and the findings strongly support the superiority and greater credibility of ROM compared to REMO. However, the fundamental question of which model, ROM or REMO, projects more plausible future ΔPr patterns, and what factors contribute to the difference, remains unanswered. Additionally, it is crucial to understand whether the mechanisms responsible for the difference between ROM and REMO in ΔPr patterns are plausible before siding with either model (James et al., 2015). Hence, in this section, we aim to explore the regional and local-scale contexts underlying various ΔPr patterns as modeled by ROM and REMO.
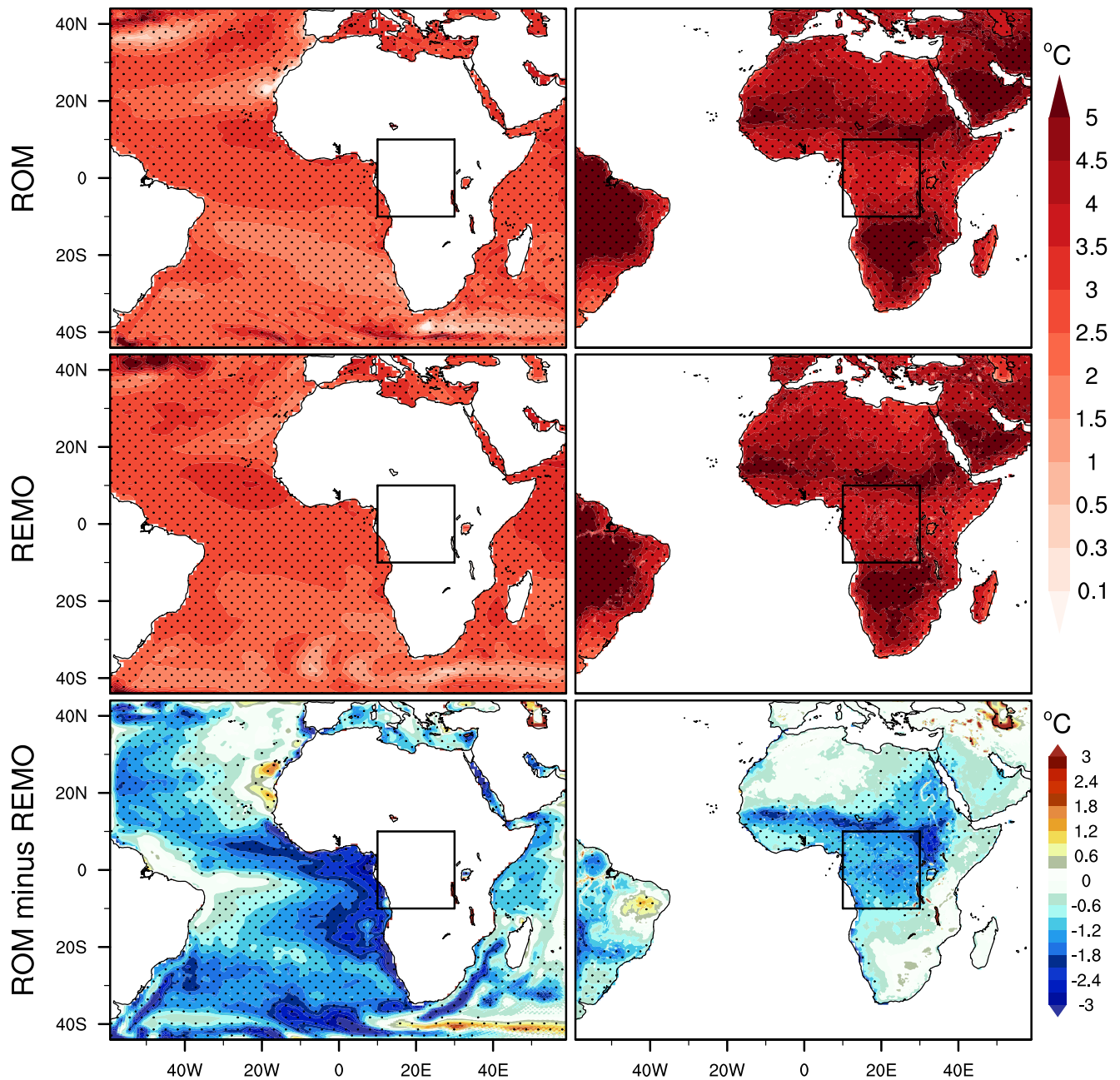
Figure 5. Changes (2070–2099 minus 1970–2000) in the climatology of mean seasonal SON sea-surface temperatures (**ΔSST** in °C; left column) and land-surface temperatures (**Δ*Ts*** in °C; right column) from ROM (1st row) and REMO (2nd row). Also shown is the future (2070–2099) difference (ROM minus REMO; 3rd row). The stippling highlight the grid points where the difference future (2070–2099) minus historical (1971–2000) of the data set under consideration (1st and 2nd rows) or the ROM minus REMO difference (third row) is statistically significant at 95% confidence level using the Student's *t*-test. The black boxes indicate the CEA.

4.1. Sea-Surface and Land-Surface Condition Changes

Variability in SSTs is an important factor of precipitation variability over CEA through direct and indirect teleconnections (Nicholson & Dezfuli, 2013). Moreover, the influence of SST anomalies on precipitation is seasonally dependent, sometimes leading to contradictory effects from one season to the next (Balas et al., 2007). However, Creese and Washington (2018) emphasized a direct relationship between eastern equatorial Atlantic SSTs and rainfall over the Congo Basin, as simulated by CMIP5 GCMs. They demonstrated that models exhibiting strong wetness over western CEA also simulate a pronounced warm SST bias and a high evaporation rate over the ocean, resulting in elevated local convection. The findings in Figure 5 and Figure S3 in Supporting

Information S1 align with these previous results. Indeed, Figure 5 shows that both ROM and REMO project enhanced SST warming over the oceans, with the mean seasonal warming level reaching $\Delta SST = 2.48°C$ for ROM and $\Delta SST = 2.71°C$ for REMO over the eastern equatorial Atlantic Ocean (20°W–10°E; 5°N–20°S). In comparison to the historical period, the coupled model ROM lowers the degree of warming by $\Delta SST = -0.23°C$ compared to REMO. Under future conditions, ROM further weakens $SSTs$ by $-1.67°C$ compared to REMO. Similarly, inland and relative to the historical period, both ROM and REMO anticipate a regional change signal of $\Delta Ts = 3.96°C$ and $\Delta Ts = 4.10°C$, respectively. Once again, ROM mitigates the level of warming compared to REMO by a value of $\Delta Ts = -0.14°C$. Under future conditions, ROM reduces Ts by a value of $-1.23°C$ compared to REMO.

Figure S3 in Supporting Information S1 unveils that the direct response of warming SSTs is enhanced evaporation ($\Delta E > 0$) over the oceans. REMO, which simulates stronger warming SSTs than ROM, also projects a higher evaporation increase. Inland, the two RCMs simulate ΔE patterns somewhat similar to ΔPr patterns. Relative to the historical period, ROM expects a mean regional increase in evaporation of 0.22 mm/day while REMO shows 0.18 mm/day. Under future conditions, the ROM minus REMO difference reveals a deficit of -0.23 mm/day on the part of ROM, in association with the lower warming degree projected by this coupled model (Figure 5). Thus, compared to the historical period, the experiment projecting a higher ΔPr (ROM) also projects higher ΔE. Similarly, under future conditions, the simulation featuring a higher rainfall amount also shows a higher evaporation amount (REMO). High ΔPr induces high ΔE, and high rainfall amount induces high evaporation amount. As evaporation is energy-limited over CEA, enhanced warming over lands as seen in Figure 5 increases the energy supply required for evaporation. Soil moisture content thereby differentiates between ROM and REMO through ΔPr or future rainfall amount. Indeed, enhanced precipitation increases soil moisture content, which, in turn, positively feeds back into evaporation through soil moisture recycling (Dirmeyer et al., 2009; Pokam et al., 2012). ROM thereby weakens Ts over CEA, in association with enhanced evaporative cooling. The water cycle is thus strengthened, with soil moisture –precipitation– serving as a differentiating factor between ROM and REMO, the required energy being assured by global warming (Seneviratne et al., 2010). ROM expects a greater increase in ΔE compared to REMO despite surface Ts weakening. This suggests that enhanced ΔPr induces greater ΔE through increased soil moisture availability, while the reverse scenario either does not occur or is limited. This is in line with previous research (e.g., Cook & Vizy, 2021; Pokam et al., 2012), which argues that although evapotranspiration is a crucial moisture source for precipitation across the Congo rainforest throughout the year, it does not govern the seasonality of rainfall.

We previously noted that compared to REMO, ROM mitigates warming over both oceans and the interior of the CEA landmass. As mentioned above, while ROM reduces the mean SSTs by $-0.23°C$, the landmass Ts is less mitigated by $-0.14°C$, meaning a reminiscence of the land-ocean thermal contrast and gradient (Longandjo & Rouault, 2020; Pokam et al., 2014). Additionally, while ROM is cooler than REMO over the CEA landmass, the two models experience almost similar Ts in most parts of the north and south of CEA, including the Sahel and Kalahari thermal lows. Similar changes are featured in sea level and surface pressure (not shown). Longandjo and Rouault (2023) highlighted the strong control of thermal contrast exercises on convection over Central Africa through precipitable water and a shallow meridional overturning circulation. The next section explores how such processes respond to changes in $SSTs$ and Ts to provide feedback on ΔPr patterns.

4.2. Atmospheric Circulation and Links to Rainfall Changes

Figure 6 shows changes in the zonal circulation within CEA, driven by changes in land-ocean thermal and pressure contrasts. We illuminate how these changes affect moisture amount entering or exiting the CEA landmass in the zonal direction by examining the vertical profile of moisture transport at the region's western (10°E) and eastern (30°E) limits. Compared to the historical period, ROM ($\Delta Qu = 10.12 \times 10^{-3}$ kg.m/kg.s) projects more enhanced moisture emanating from low-level (1,000–850 hPa) westerlies (Pokam et al., 2014) than REMO ($\Delta Qu = 8.70 \times 10^{-3}$ kg.m/kg.s) at the western boundary. In contrast, at the eastern boundary, moisture advection from low-level easterlies (Munday et al., 2021) is expected to reduce further in ROM ($\Delta Qu = -4 \times 10^{-3}$ kg.m/kg.s) than in REMO ($\Delta Qu = -2.51 \times 10^{-3}$ kg.m/kg.s). Under future conditions, the difference ROM minus REMO unveils that enhancement in low-level westerlies' moisture from the west ($\Delta Qu = 1.43 \times 10^{-3}$ kg.m/kg.s) almost offsets the weakening in low-level easterlies' moisture at the east ($\Delta Qu = -1.48 \times 10^{-3}$ kg.m/kg.s), leading to compensating effects between ROM and REMO. In the middle and upper layers (>700 hPa), ROM and REMO exhibit similar changes both at the west ($\Delta Qu = -4.75 \times 10^{-3}$ and -4.94×10^{-3} kg.m/kg.s, respectively) and east
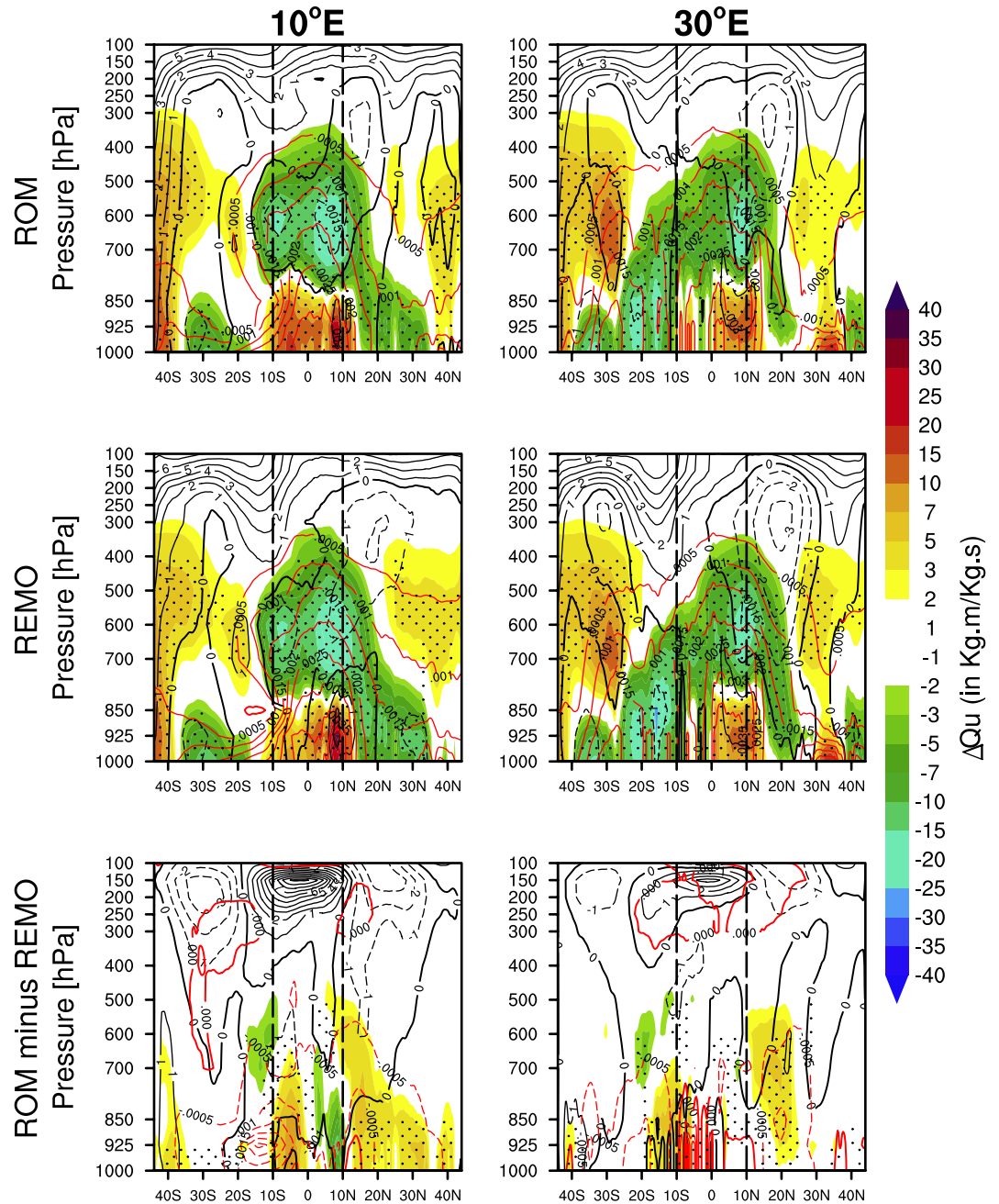
Figure 6. Latitude-height cross-section of changes (2070–2099 minus 1971–2000) in the zonal-mean zonal moisture transport ΔQu (color in shaded; kg.m/kg.s), zonal wind Δu (black contours; m/s), and specific humidity Δq (red contours; kg/kg) at the western boundary (10°E, first column) and eastern boundary (30°E, second column) of CEA from ROM (first row) and REMO (second row). The difference ROM minus REMO is also shown under future conditions (2070–2099; third row). Positive change values are shown in solid contours while negative values are shown in dashed. The stippling highlight the grid points where the difference future (2070–2099) minus historical (1971–2000) of the data set under consideration (1st and 2nd rows) or the ROM minus REMO difference (3rd row) is statistically significant at 95% confidence level using the Student's t-test. Vertical bars delimit the CEA's latitudinal band (10°S–10°N).

($\Delta Qu = -3.20 \times 10^{-3}$ and -3.16×10^{-3} kg.m/kg.s, respectively). Moreover, the difference ROM minus REMO under future conditions is minimal both at the west ($\Delta Qu = 0.19 \times 10^{-3}$ kg.m/kg.s) and east (-0.04×10^{-3} kg.m/kg.s). These results suggest that the zonal circulation influences ΔPr patterns through low-level circulations. However, the zonal circulation does not differentiate between ROM and REMO in ΔPr patterns.
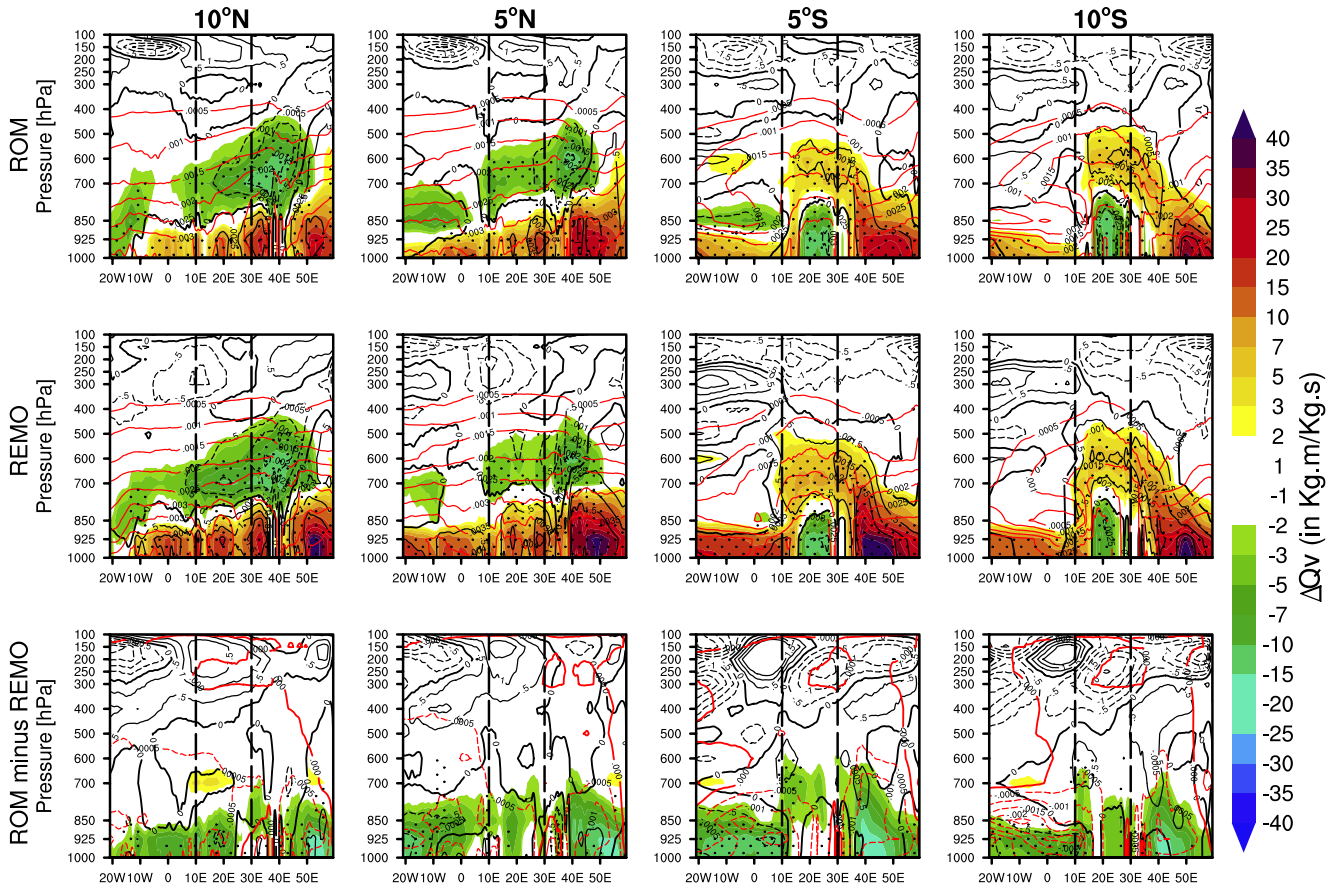
Figure 7. Longitude-height cross-section of changes (2070–2099 minus 1971–2000) in the meridional-mean meridional moisture transport ΔQv (color in shaded; kg.m/kg.s), changes in meridional wind Δv (black contours; m/s) and specific humidity Δq (red contours; kg/kg) at 10°N (first column), 5°N (second column), 5°S (third column), and 10°S (fourth column) from ROM (first row) and REMO (second row). The difference ROM minus REMO is also shown under future conditions (2070–2099; third row). Positive change values are shown in solid contours while negative values are shown in dashed. The stippling highlight the grid points where the difference future (2070–2099) minus historical (1971–2000) of the data set under consideration (1st and 2nd rows) or the ROM minus REMO difference (third row) is statistically significant at 95% confidence level using the Student's t-test. Vertical bars delimit the CEA's longitudinal band (10°–30°E).

In the meridional direction, ROM and REMO exhibit contrasting mechanisms by which the shallow meridional overturning circulation (Longandjo & Rouault, 2023) reacts to shape ΔPr patterns (Figure 7), in association with modifications in surface temperatures. Since the typical circulation pattern over CEA comprises low-tropospheric convergence (1,000–850 hPa) overlaid by mid-tropospheric divergence (850–500 hPa) (Pokam et al., 2012), we have split the analyses into these two layers. Relative to the historical period and in lower layers, on the northern side at 5°N, ROM projects an enhanced northward moisture transport by $\Delta Qv = 7.09 \times 10^{-3}$ kg.m/kg.s which weakens at 10°N up to $\Delta Qv = 5.53 \times 10^{-3}$ kg.m/kg.s. REMO expects $\Delta Qv = 9.76 \times 10^{-3}$ kg.m/kg.s at 5°N, but this strengthens at 10°N to $\Delta Qv = 9.98 \times 10^{-3}$ kg.m/kg.s. Under future conditions, compared to REMO, ROM features a deficit in northward moisture transport at 5°N of $\Delta Qv = -2.68 \times 10^{-3}$ kg.m/kg.s, which strengthens at 10°N to reach $\Delta Qv = -4.44 \times 10^{-3}$ kg.m/kg.s. On the southern side, ROM expects enhanced southward moisture transport of $\Delta Qv = -3.90 \times 10^{-3}$ kg.m/kg.s at 5°S, which strengthens to $\Delta Qv = -5.33 \times 10^{-3}$ kg.m/kg.s at 10°S. In contrast, REMO projects $\Delta Qv = -2.29 \times 10^{-3}$ kg.m/kg.s at 5°S, which weakens to $\Delta Qv = -1.53 \times 10^{-3}$ kg.m/kg.s at 10°S. Finally, the future difference ROM minus REMO yields $\Delta Qv = -1.62 \times 10^{-3}$ kg.m/kg.s at 5°S and $\Delta Qv = -3.79 \times 10^{-3}$ kg.m/kg.s at 10°S. Thus, ROM simulates more moisture transport that recirculates within the region than REMO on the northern side, but the situation is reversed on the southern side. A similar analysis in the middle layers shows that REMO simulates more moisture inflow into the region than ROM (see Text S1 in Supporting Information S1), despite this experiment projecting lesser wetness than ROM compared to the historical period. This is because of the axis of circulation in the middle layers (Figure S4 in Supporting Information S1), in association with changes in the intensity of AEJs (Figure S5 in Supporting Information S1). In
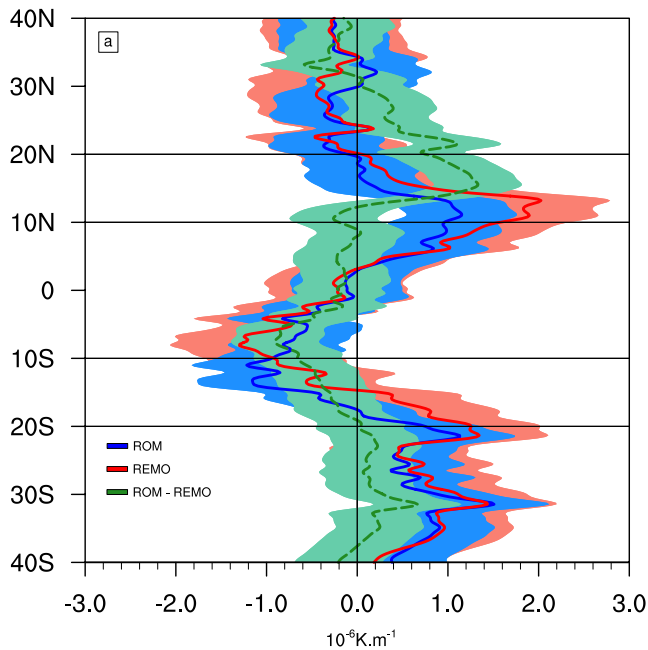
Figure 8. Changes (2070–2099 minus 1971–2000) in the SON climatology of the latitudinal migration of the 850 hPa temperature gradient (in 10^{-6} K/m), averaged over the longitudes 10°W–30°E, from ROM (blue) and REMO (red). The difference (ROM minus REMO) under the future period is also depicted (dashed green line). The corresponding shaded area in color represents the standard deviation, indicating the variability in the temperature gradient. Horizontal black bars denote latitudes 10°S, 5°S, 5°N, and 10°N, while the vertical bar represents the gradient value 0.

response to enhanced southward and northward surface temperature gradients (Figure 8), the two components of the AEJ (Jackson et al., 2009) also strengthen. However, the main difference between ROM and REMO lies in the fact that the latter experiment did not detect the AEJ-S during the historical period. Therefore, the jet–rainfall coupling in its projection is not opposed to its historical counterpart. This result further endorses our preceding argument that historical biases strongly affect REMO's projections.

The above-described processes are conclusive with the increase in precipitation projected by both ROM and REMO. The enhancement in zonal circulation at the west, which is differentiated in the lower layers between ROM and REMO, aligns with the strengthened land-ocean thermal and pressure contrasts. Figure 6 also illustrates that the two models project an increase in specific humidity. Such conditions favor deep convection over CEA through the interplay between the Congo Basin cell and precipitable water (Longandjo & Rouault, 2023). This argument is further supported by the expectation of a reinforced Congo Basin cell in both models, with ROM exhibiting $\Delta \Psi Z = -3.93 \times 10^{11}$ kg/s and REMO showing $\Delta \Psi Z = -2.67 \times 10^{11}$ kg/s. In addition, ROM and REMO anticipate enhanced northern and southern shallow Hadley cells. This shallow cell appears to be the factor that distinguishes between ROM and REMO in ΔPr patterns, as these models simulate almost similar changes in the deep Hadley cell (Figure 7; $\Delta \Psi M = -0.67 \times 10^{11}$ kg/s for ROM and $\Delta \Psi M = -0.69 \times 10^{11}$ kg/s for REMO) and zonal circulation (Figure 6). While the change, compared to the historical period, in northward moisture transport strengthens at 10°N in REMO (indicating increased outflows), it weakens in ROM (suggesting decreased outflows). An opposite situation characterizes the change in moisture transport on the southern side. This implies that ROM anticipates a wetter condition relative to the historical period compared to REMO, associated with a projected weaker northern Hadley cell, which limits outflows toward the Sahel (Figure S6 in Supporting Information S1). Contrastingly, ROM projects a stronger southern Hadley cell than REMO, enhancing outflows toward southern Africa.

These processes of change align with earlier findings by Longandjo and Rouault (2023). Specifically, the Sahel thermal low drives the northern shallow Hadley cell, while the Kalahari low plays a similar role for the southern shallow Hadley cell through the northward and southward meridional thermal gradients, respectively. Figure 8 shows that, compared to the historical period, ROM projects a weaker enhancement of the surface temperature gradient than REMO between the northern CEA and the Sahel low (within 10°–20°N). Conversely, ROM projects a stronger increased surface temperature gradient than REMO between the southern CEA and the Kalahari low (within 10°–20°S). This result is consistent with the fact that—although ROM mitigates warming compared to REMO—the projection based on ROM better simulates the warmer nature of the Kalahari low than the Sahel low at this time of the year (Figure S7 in Supporting Information S1). To completely illuminate the plausibility of these mechanisms, further investigation into the way moisture flux divergence and its components feature the shallow meridional circulation is needed, which is the focus of the next section.

4.3. Moisture Flux Divergence and Links to Rainfall Changes

Figure 9 illustrates that, compared to the historical period, both ROM and REMO consistently project a weakened moisture flux convergence $[\nabla \cdot (qV) < 0]$ typically occurring at low levels of CEA. There is also a consistent weakening in the moisture flux divergence $[\nabla \cdot (qV) > 0]$ in the middle layers, which generally overlays the convergence in lower layers. However, while REMO (Figure 9b) expects a more enhanced moisture flux convergence in the lower layers compared to ROM (Figure 9a), both experiments project an equal increase in convergence in the middle layers. Analysis of the difference ROM minus REMO under future conditions (Figure 9c) reveals that ROM (REMO) is more divergent (convergent) than REMO (ROM) in the lower (middle) layers. Therefore, compared to the historical period, moisture surplus—responsible for wetter conditions in ROM than in REMO—results from mid-tropospheric moisture flux convergence. This finding supports previous
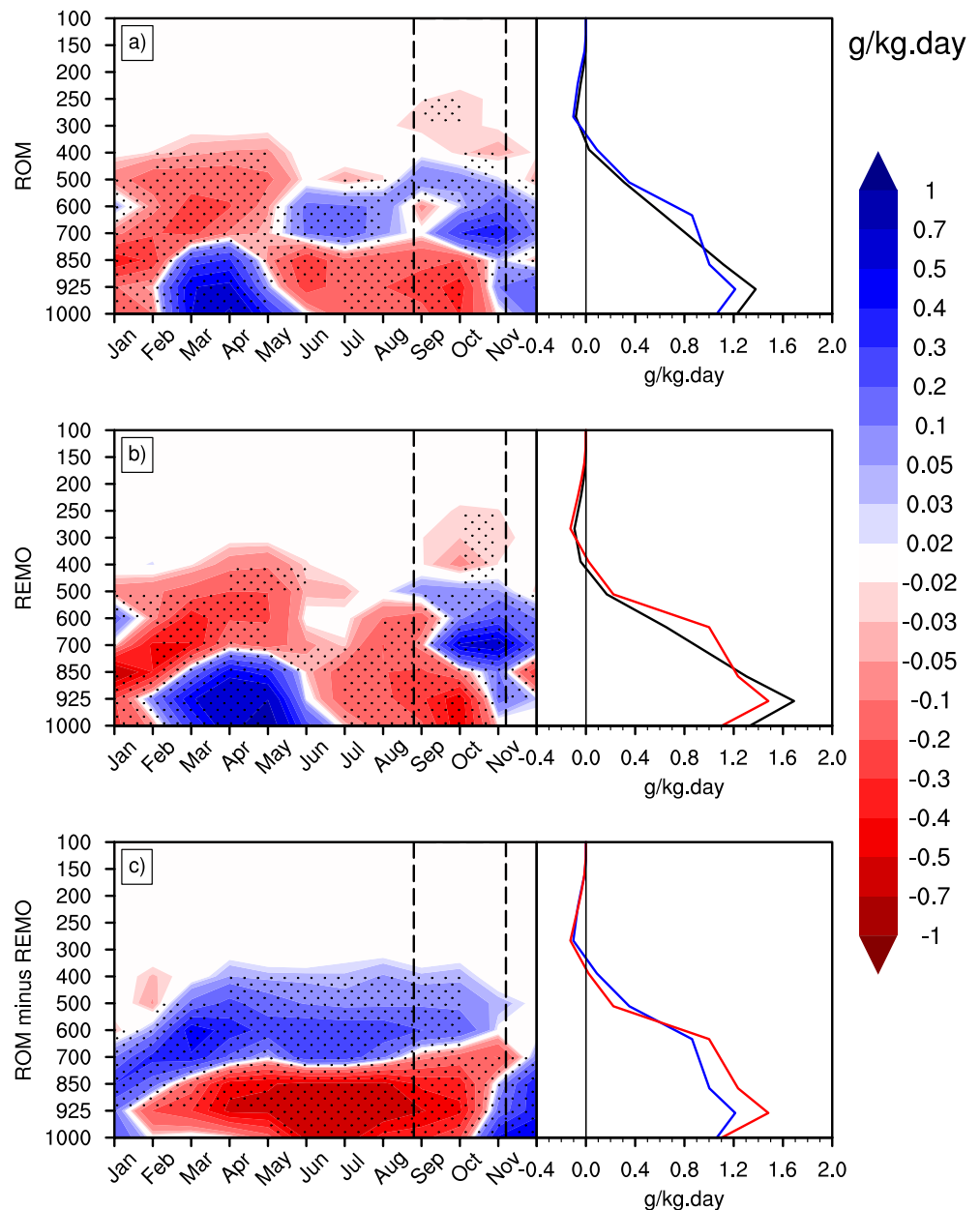
Figure 9. Changes in the seasonality of the vertical profile of moisture flux divergence $[\nabla \cdot (qV)]$ (left) and mean SON $[\nabla \cdot (qV)]$ change shown in line plots (right) from ROM (top panel) and REMO (middle panel). The future (2070–2099) difference between ROM and REMO is also displayed in the bottom panel. The stippling highlights the grid points where the difference future (2070–2099) minus historical (1971–2000) of the data set under consideration (a and b) or the ROM minus REMO difference (c) is statistically significant at 95% confidence level using the Student's t-test.

research by Longandjo and Rouault (2023), who also identified mid-tropospheric moisture convergence as responsible for precipitating convection. Furthermore, in line with these authors, examining Figures 10 and 11 supports moisture convergence $[q\nabla \cdot V]$ (Figure 10) as the main component shaping $\nabla \cdot (qV)$ and thereby responsible for ΔPr patterns. Indeed, the pattern of changes in $q\nabla \cdot V$ is similar to that of $\nabla \cdot (qV)$. However, changes in moisture advection $[V\nabla \cdot q]$ (Figure 11) indicate that ROM expects reduced advection in both the lower and middle layers, whereas REMO projects increased advection. The moisture convergence that historically drives the precipitation climatology also drives the projected changes. The strengthening of moisture convergence in the middle layers in ROM aligns with the weakening of its northern shallow meridional circulation, which restricts outflows toward the Sahel.
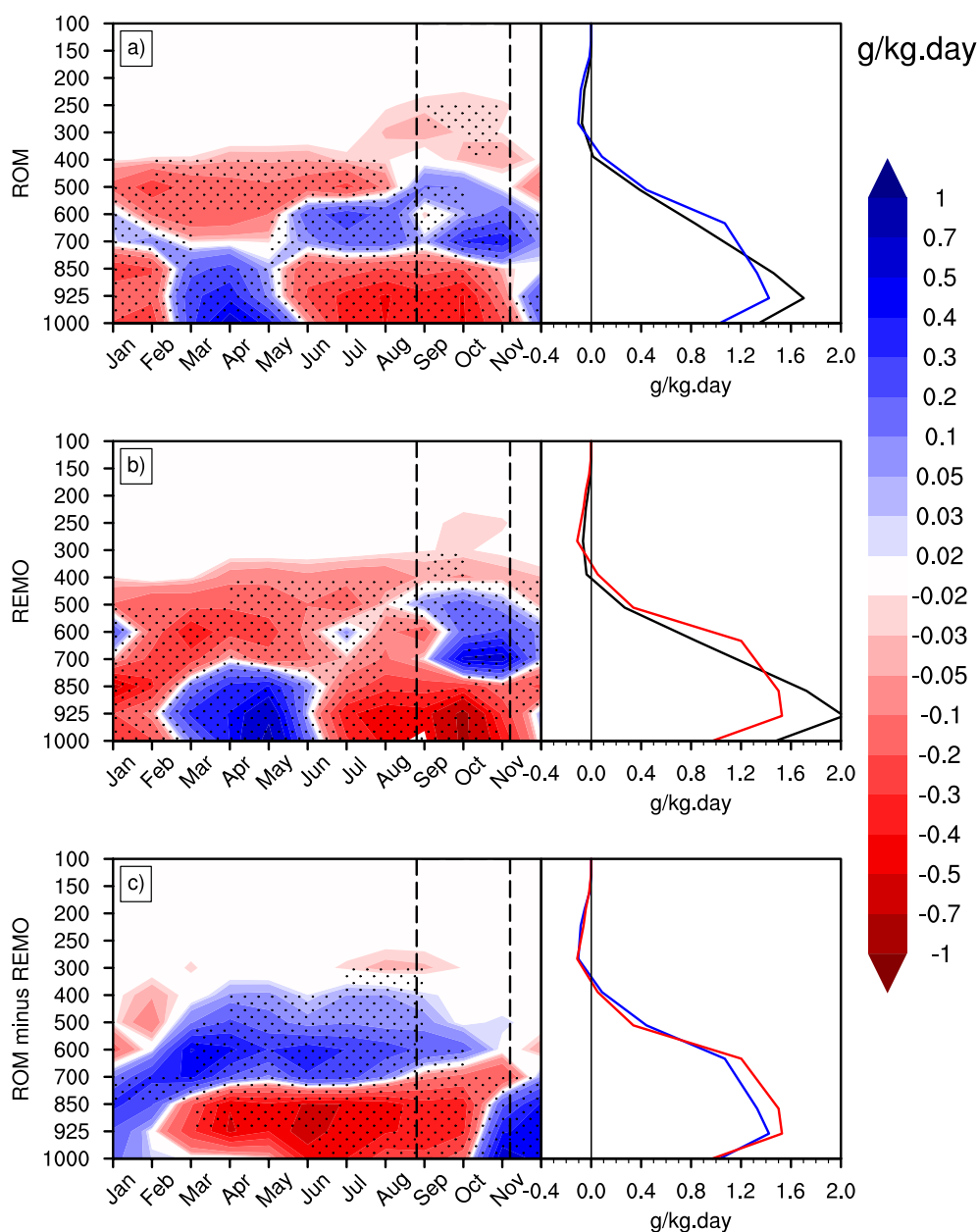
Figure 10. Same as in Figure 9, but for the moisture convergence [$q\nabla \cdot V$].

A similar process governs precipitation climatology in ROM and REMO under future conditions. Figures 9–11 also demonstrate that mid-tropospheric moisture divergence continues to cap the moisture convergence in the lower layers. The disparities in future rainfall climatologies between ROM and REMO are also linked to the moisture convergence component. Overall, the effect of warming mitigation as simulated by ROM leads to a reduction of the moisture advection component, in line with, at least, the expectations of the Clausius-Clapeyron relationship (Chadwick et al., 2013). Under future conditions, the southward meridional surface temperature gradient in REMO enhances enough to reveal the AEJ-S component (absent in the historical simulation), thereby improving the jet–rainfall coupling (Whittleston et al., 2017). The presence of the AEJ-S further contributes to moistening mid-tropospheric layers, although Longandjo and Rouault (2023) argued that the contribution of jets to the overall mid-tropospheric layers' moisture convergence is small.
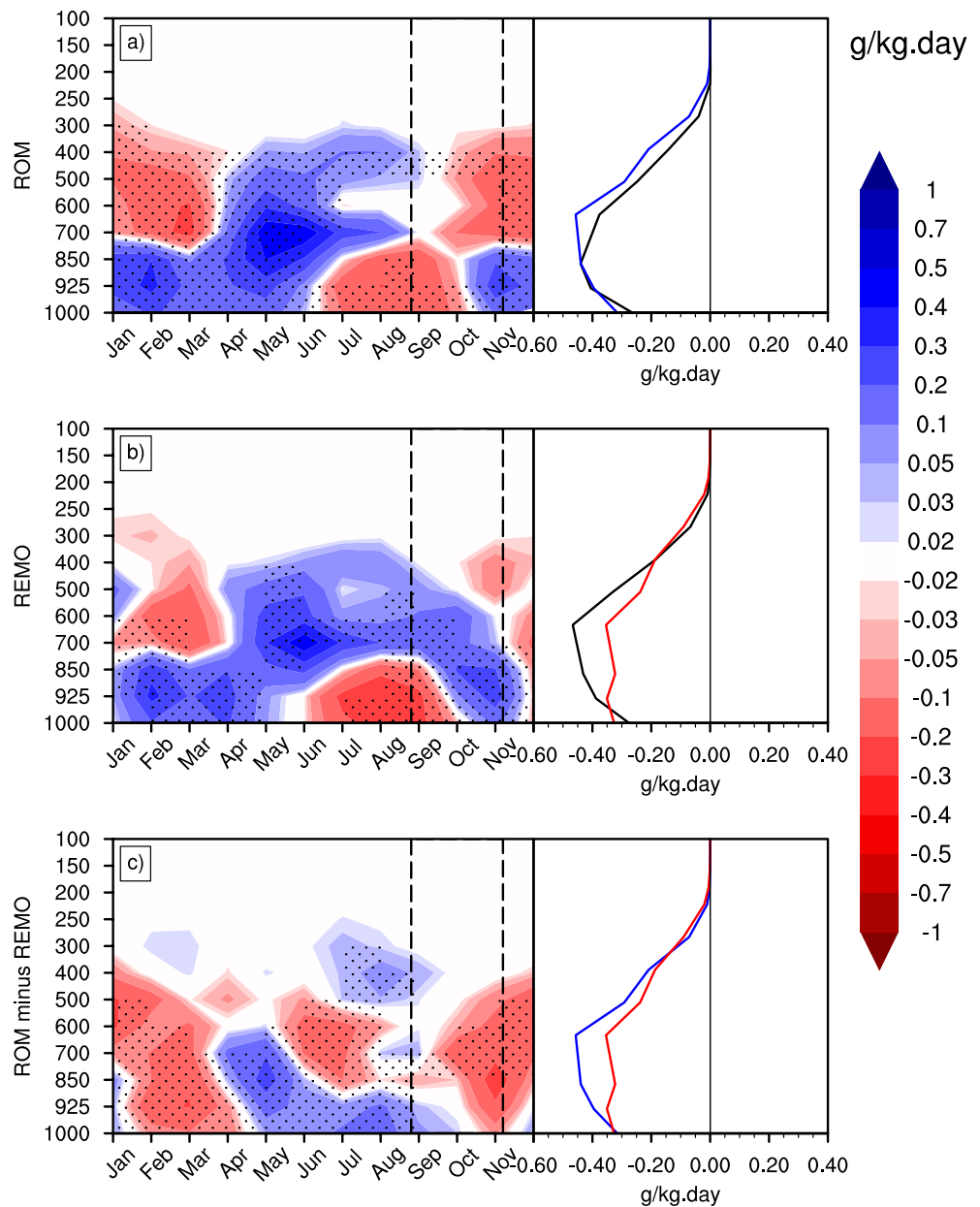
Figure 11. Same as Figure 9, but for the moisture advection $[V\nabla \cdot q]$.

5. Discussion and Conclusions

The regionally coupled model ROM and its atmospheric component REMO project increased rainfall ($\Delta Pr > 0$) in most parts of CEA by the late twenty-first century relative to the late twenty-first century. In comparison to the historical period, ROM expects a stronger precipitation increase than REMO, despite REMO simulating a higher total precipitation amount under future conditions. Changes in SSTs and Ts, along with reminiscent historical biases in the standalone atmospheric model REMO (Tamoffo, Weber, Cabos, Sein, et al., 2024) trigger modifications in the physical processes underpinning ΔPr patterns. The potential mechanisms, highlighted as drivers of ΔPr patterns, also differentiate between ROM and REMO projections and aid in discriminating the plausibility of ROM's ΔPr pattern.

We found that the coupled model ROM cools future temperatures compared to the atmospheric model REMO, particularly evident in eastern equatorial Atlantic Ocean SSTs compared to the CEA landmass Ts. The

evaporative cooling is at play in reducing Ts over CEA under coupling configuration. This leads to an enhanced water cycle with soil moisture acting as the forcing factor through increased rainfall and the warming providing the energy surplus. Simultaneously, changes over the Sahel and Kalahari thermal lows do not substantially differentiate between ROM and REMO, apart from the better depiction by ROM of the warmer Kalahari low than the Sahel low. As a result, dipole-like land-ocean thermal contrast and subsequent pressure contrast (Longandjo & Rouault, 2020; Pokam et al., 2014) are maintained and intensified. The resulting strengthened Congo Basin cell augments precipitable water over CEA through increased specific humidity. Additionally, changes in the regional shallow meridional overturning circulation, forced by changes in typical positive northward (10°–20°N) and negative southward (10°–20°S) temperature gradients (Longandjo & Rouault, 2023; Zhang et al., 2008), underlie both models' ΔPr patterns and differentiate between ROM and REMO. While both models expect enhanced northward and southward thermal gradients, REMO exhibits greater strength in the north and comparatively weaker strength in the south. Consequently, the northern shallow Hadley cell and subsequent northward moisture transport are more robust in REMO than in ROM, with opposite trends in the southern hemisphere. Relative to the historical period, ROM shows a weaker northern shallow Hadley cell compared to REMO, limiting outflows toward the Sahel, and increasing the likelihood of moisture flux convergence within the region. This process explains more wetness featuring ROM compared to REMO, relative to the historical period. The same process is linked to higher rainfall amounts in REMO under future conditions. Both models project a reduction in typical low-level moisture flux convergence [$\Delta(\nabla \cdot (qV)) < 0$] over CEA, alongside a weakening in mid-tropospheric moisture flux divergence [$\Delta(\nabla \cdot (qV)) > 0$]. This indicates that enhanced mid-tropospheric moisture flux convergence primarily influences enhanced precipitation ($\Delta Pr > 0$), consistent with recent findings by Longandjo and Rouault (2023), who highlight the role of mid-tropospheric moisture convergence in precipitating convection over Central Africa. Our analysis also indicates that changes in moisture convergence ($q\nabla \cdot V$) predominate over changes in moisture advection ($V\nabla \cdot q$) in the total $\nabla \cdot (qV)$, aligning with previous results by Cook and Vizy (2021).

Several findings highlighted above allow advocating for the more plausible ROM's ΔPr pattern. Firstly, ROM adds value compared to REMO under historical climate conditions for the right reasons, as demonstrated by Tamoffo, Weber, Cabos, Sein, et al. (2024). Secondly, the mechanisms underlying ΔPr patterns are consistent with those underpinning observed climatology, as identified across observational and reanalysis data sets, and ROM better depicts some of them. For instance, Probability Density Functions reveal that the shapes of precipitation distributions based on ROM closely resemble those of observations and the ERA5 reanalysis, compared to distributions based on REMO, across both historical and future periods. We also noted that the overall processes driving ΔPr patterns align with the moisture-convergence-controlled regime occurring in the rainy season, as demonstrated by Longandjo and Rouault (2023). Thirdly, the Sahel and Kalahari thermal lows play a pivotal role in shaping ΔPr patterns in both ROM and REMO, yet ROM provides a more accurate portrayal of the warmer nature of the Kalahari low compared to the Sahel low. The future projection of the southern jet–rainfall coupling (Whittleston et al., 2017) is opposed to its historical counterpart in ROM, but this is not the case for REMO, which lacks the jet–rainfall coupling process under the historical climate. This casts doubt on the rainfall change-related modifications in the AEJ-S.

The present study demonstrates the necessity of accounting for ocean-atmospheric interactions in regional climate models to refine regional climate information provided to policymakers. It is important to highlight that the robustness of these findings requires additional evaluation. Our study exclusively examines the outcomes of a single dynamically downscaled ESM using an RCM in its coupled and uncoupled version. Further investigations should encompass additional RCMs operating in both modes, each driven by a variety of ESMs.

Conflict of Interest

The authors declare no conflicts of interest relevant to this study.

Data Availability Statement

The model simulations were performed at the German Climate Computing Center (Deutsches Klimarechenzentrum, DKRZ) in Hamburg. All observational and reanalysis data used in this study are publicly available at no charge and with unrestricted access. The ERA5 reanalysis is produced within the Copernicus Climate

Change Service (C3S) by the ECMWF and is accessible via the link https://cds.climate.copernicus.eu/cdsapp#!/dataset/reanalysis-era5-pressure-levels-monthly-means?tab1⁄4form; the GPCC observational data set is available at https://opendata.dwd.de/climate_environment/GPCC/html/fulldata-monthly v2020y doiy download.html; the CRU-v4.04 data set is available at https://data.ceda.ac.uk/badc/cru/data/cru_ts/cru_ts_4.05/data/pre (Harris et al., 2020); the CHIRPS2 data are available at https://data.chc.ucsb.edu/products/CHIRPS-2.0/global_daily/netcdf/.

References

Balas, N., Nicholson, S. E., & Klotter, D. (2007). The relationship of rainfall variability in West Central Africa to sea-surface temperature fluctuations. *International Journal of Climatology*, *27*(10), 1335–1349. https://doi.org/10.1002/joc.1456

Band, S. S., Karami, H., Jeong, Y.-W., Moslemzadeh, M., Farzin, S., Chau, K.-W., et al. (2022). Evaluation of time series models in simulating different monthly scales of drought index for improving their forecast accuracy. *Frontiers in Earth Science*, *10*. https://doi.org/10.3389/feart.2022.839527

Bangelesa, F., Abel, D., Pollinger, F., Rai, P., Ziegler, K., Ebengo, D., et al. (2023). Projected changes in rainfall amount and distribution in the Democratic Republic of Congo—Evidence from an ensemble of high-resolution climate simulations. *Weather and Climate Extremes*, *42*, 100620. https://doi.org/10.1016/j.wace.2023.100620

Cabos, W., Sein, D., de la Vara, A., & Alvarez Garcia, F. (2020). *Impact of ocean-atmosphere coupling on regional climate: The Iberian Peninsula case*. Copernicus GmbH. https://doi.org/10.5194/egusphere-egu2020-13098

Cabos, W., Sein, D. V., Pinto, J. G., Fink, A. H., Koldunov, N. V., Alvarez, F., et al. (2017). The South Atlantic Anticyclone as a key player for the representation of the tropical Atlantic climate in coupled climate models. *Climate Dynamics*, *48*(11Â–12), 4051–4069. https://doi.org/10.1007/s00382-016-3319-9

Chadwick, R., Boutle, I., & Martin, G. (2013). Spatial patterns of precipitation change in CMIP5: Why the rich do not get richer in the tropics. *Journal of Climate*, *26*(11), 3803–3822. https://doi.org/10.1175/jcli-d-12-00543.1

Cook, K. H., & Vizy, E. K. (2021). Hydrodynamics of regional and seasonal variations in Congo Basin precipitation. *Climate Dynamics*, *59*(5–6), 1775–1797. https://doi.org/10.1007/s00382-021-06066-3

Creese, A., & Washington, R. (2018). A process-based assessment of CMIP5 rainfall in the Congo Basin: The September–November rainy season. *Journal of Climate*, *31*(18), 7417–7439. https://doi.org/10.1175/jcli-d-17-0818.1

Creese, A., Washington, R., & Jones, R. (2019). Climate change in the Congo Basin: Processes related to wetting in the December–February dry season. *Climate Dynamics*, *53*(5–6), 3583–3602. https://doi.org/10.1007/s00382-019-04728-x

Creese, A., Washington, R., & Munday, C. (2019). The plausibility of September–November Congo Basin rainfall change in coupled climate models. *Journal of Geophysical Research: Atmospheres*, *124*(11), 5822–5846. https://doi.org/10.1029/2018jd029847

Dirmeyer, P. A., Schlosser, C. A., & Brubaker, K. L. (2009). Precipitation, recycling, and land memory: An integrated analysis. *Journal of Hydrometeorology*, *10*(1), 278–288. https://doi.org/10.1175/2008jhm1016.1

Doblas-Reyes, F. J., Sörensson, A. A., Almazroui, M., Dosio, A., Gutowski, W. J., Haarsma, R., et al. (2021). Linking global to regional climate change. In V. Masson-Delmotte, P. Zhai, A. Pirani, S. L. Connors, C. Péan, S. Berger, et al. (Eds.), *Climate Change 2021: The Physical Science Basis. Contribution of Working Group I to the Sixth Assessment Report of the Intergovernmental Panel on Climate Change* (pp. 1363–1512). Cambridge University Press. https://doi.org/10.1017/9781009157896.012

d'Orgeval, T. (2008). Impact du changement climatique sur la saison des pluies en Afrique de l'Ouest: Que nous disent les modèles de climat actuels? *Science et Changements Planétaires / Sécheresse*, *19*(2), 79–85.

Dosio, A., Jury, M. W., Almazroui, M., Ashfaq, M., Diallo, I., Engelbrecht, F. A., et al. (2021). Projected future daily characteristics of African precipitation based on global (CMIP5, CMIP6) and regional (CORDEX, CORDEX-CORE) climate models. *Climate Dynamics*, *57*(11–12), 3135–3158. https://doi.org/10.1007/s00382-021-05859-w

Dosio, A., Turner, A. G., Tamoffo, A. T., Sylla, M. B., Lennard, C., Jones, R. G., et al. (2020). A tale of two futures: Contrasting scenarios of future precipitation for West Africa from an ensemble of regional climate models. *Environmental Research Letters*, *15*(6), 064007. https://doi.org/10.1088/1748-9326/ab7fde

Funk, C., Peterson, P., Landsfeld, M., Pedreros, D., Verdin, J., Shukla, S., et al. (2015). The climate hazards infrared precipitation with stations—A new environmental record for monitoring extremes [Dataset]. *Scientific Data*, *2*(1), 150066. https://doi.org/10.1038/sdata.2015.66

Giorgetta, M. A., Jungclaus, J., Reick, C. H., Legutke, S., Bader, J., Böttinger, M., et al. (2013). Climate and carbon cycle changes from 1850 to 2100 in MPI-ESM simulations for the Coupled Model Intercomparison Project phase 5. *Journal of Advances in Modeling Earth Systems*, *5*(3), 572–597. https://doi.org/10.1002/jame.20038

Harris, I., Osborn, T. J., Jones, P., & Lister, D. (2020). Version 4 of the CRU TS monthly high-resolution gridded multivariate climate dataset [Dataset]. *Scientific Data*, *7*(1), 109. https://doi.org/10.1038/s41597-020-0453-3

Hersbach, H., Bell, B., Berrisford, P., Hirahara, S., Horányi, A., Muñoz-Sabater, J., et al. (2020). The ERA5 global reanalysis [Dataset]. *Quarterly Journal of the Royal Meteorological Society*, *146*(730), 1999–2049. https://doi.org/10.1002/qj.3803

Jackson, B., Nicholson, S. E., & Klotter, D. (2009). Mesoscale convective systems over western equatorial Africa and their relationship to large-scale circulation. *Monthly Weather Review*, *137*(4), 1272–1294. https://doi.org/10.1175/2008mwr2525.1

Jacob, D. (2001). The role of water vapour in the atmosphere. A short overview from a climate modeller's point of view. *Physics and Chemistry of the Earth*, *26*(6–8), 523–527. https://doi.org/10.1016/s1464-1895(01)00094-1

Jacob, D., Elizalde, A., Haensler, A., Hagemann, S., Kumar, P., Podzun, R., et al. (2012). Assessing the transferability of the regional climate model REMO to different coordinated regional climate downscaling experiment (CORDEX) regions. *Atmosphere*, *3*(1), 181–199. https://doi.org/10.3390/atmos3010181

Jacob, D., Van den Hurk, B. J. J. M., Andrae, U., Elgered, G., Fortelius, C., Graham, L. P., et al. (2001). A comprehensive model inter-comparison study investigating the water budget during the BALTEX-PIDCAP period. *Meteorology and Atmospheric Physics*, *77*(1–4), 19–43. https://doi.org/10.1007/s007030170015

James, R., Washington, R., Abiodun, B., Kay, G., Mutemi, J., Pokam, W., et al. (2018). Evaluating climate models with an African lens. *Bulletin of the American Meteorological Society*, *99*(2), 313–336. https://doi.org/10.1175/bams-d-16-0090.1

James, R., Washington, R., & Jones, R. (2015). Process-based assessment of an ensemble of climate projections for West Africa. *Journal of Geophysical Research: Atmospheres*, *120*(4), 1221–1238. https://doi.org/10.1002/2014jd022513

Jungclaus, J. H., Fischer, N., Haak, H., Lohmann, K., Marotzke, J., Matei, D., et al. (2013). Characteristics of the ocean simulations in the Max Planck Institute Ocean Model (MPIOM) the ocean component of the MPI-Earth system model. *Journal of Advances in Modeling Earth Systems*, *5*(2), 422–446. https://doi.org/10.1002/jame.20023

Kay, A. L., Davies, H. N., Bell, V. A., & Jones, R. G. (2008). Comparison of uncertainty sources for climate change impacts: Flood frequency in England. *Climatic Change*, *92*(1–2), 41–63. https://doi.org/10.1007/s10584-008-9471-4

King, J. A., Washington, R., & Engelstaedter, S. (2020). Representation of the Indian Ocean Walker circulation in climate models and links to Kenyan rainfall. *International Journal of Climatology*, *41*(S1). https://doi.org/10.1002/joc.6714

Kirtman, B., Power, S. B., Adedoyin, J. A., Boer, G. J., Bojariu, R., Camilloni, I., et al. (2013). Near-term Climate Change: Projections and Predictability. In *Climate Change 2013: The Physical Science Basis. Contribution of Working Group I to the Fifth Assessment Report of the Intergovernmental Panel on Climate Change* (Vol. 9781107057, pp. 953–1028). Cambridge University Press.

Kuete, G., Pokam Mba, W., & Washington, R. (2019). African easterly jet south: Control, maintenance mechanisms and link with southern subtropical waves. *Climate Dynamics*, *54*(3–4), 1539–1552. https://doi.org/10.1007/s00382-019-05072-w

Laux, P., Dieng, D., Portele, T. C., Wei, J., Shang, S., Zhang, Z., et al. (2021). A high-resolution regional climate model physics ensemble for northern sub-Saharan Africa. *Frontiers in Earth Science*, *9*. https://doi.org/10.3389/feart.2021.700249

Lee, J.-Y., Marotzke, J., Bala, G., Cao, L., Corti, S., Dunne, J. P., et al. (2021). Future global climate: Scenario-based projections and near-term information. In V. Masson-Delmotte, P. Zhai, A. Pirani, S. L. Connors, C. Péan, S. Berger, et al. (Eds.), *Climate Change 2021: The Physical Science Basis. Contribution of Working Group I to the Sixth Assessment Report of the Intergovernmental Panel on Climate Change* (pp. 553–672). Cambridge University Press. https://doi.org/10.1017/9781009157896.006

Lloyd-Hughes, B., & Saunders, M. A. (2002). A drought climatology for Europe. *International Journal of Climatology*, *22*(13), 1571–1592. https://doi.org/10.1002/joc.846

Longandjo, G.-N. T., & Rouault, M. (2020). On the structure of the regional-scale circulation over Central Africa: Seasonal evolution, variability, and mechanisms. *Journal of Climate*, *33*(1), 145–162. https://doi.org/10.1175/jcli-d-19-0176.1

Longandjo, G.-N. T., & Rouault, M. (2023). *Revisiting the seasonal cycle of rainfall over Central Africa*. Research Square Platform LLC. https://doi.org/10.21203/rs.3.rs-2956778/v1

Longandjo, G.-N. T., & Rouault, M. (2024). Revisiting the seasonal cycle of rainfall over central africa. *Journal of Climate*, *37*(3), 1015–1032. https://doi.org/10.1175/jcli-d-23-0281.1

Majewski, D. (1991). The EUROPA-model of the Deutscher Wetterdienst. In *Proc. Seminar on Numerical Methods in Atmospheric Models. Reading, United Kingdom, ECMWF* (pp. 147–191).

Monerie, P.-A., Sanchez-Gomez, E., & Boé, J. (2016). On the range of future Sahel precipitation projections and the selection of a sub-sample of CMIP5 models for impact studies. *Climate Dynamics*, *48*(7–8), 2751–2770. https://doi.org/10.1007/s00382-016-3236-y

Monerie, P.-A., Wainwright, C. M., Sidibe, M., & Akinsanola, A. A. (2020). Model uncertainties in climate change impacts on Sahel precipitation in ensembles of CMIP5 and CMIP6 simulations. *Climate Dynamics*, *55*(5–6), 1385–1401. https://doi.org/10.1007/s00382-020-05332-0

Munday, C., Washington, R., & Hart, N. (2021). African low-level jets and their importance for water vapor transport and rainfall. *Geophysical Research Letters*, *48*(1). https://doi.org/10.1029/2020gl090999

Neelin, J. D., Krasting, J. P., Radhakrishnan, A., Liptak, J., Jackson, T., Ming, Y., et al. (2023). Process-Oriented diagnostics: Principles, practice, community development, and common standards. *Bulletin of the American Meteorological Society*, *104*(8), E1452–E1468. https://doi.org/10.1175/bams-d-21-0268.1

Nicholson, S. E., & Dezfuli, A. K. (2013). The relationship of rainfall variability in Western Equatorial Africa to the tropical oceans and atmospheric circulation. Part I: The Boreal Spring. *Journal of Climate*, *26*(1), 45–65. https://doi.org/10.1175/jcli-d-11-00653.1

Nicholson, S. E., & Grist, J. P. (2003). The seasonal evolution of the atmospheric circulation over West Africa and Equatorial Africa. *Journal of Climate*, *16*(7), 1013–1030. https://doi.org/10.1175/1520-0442(2003)016<1013:tseota>2.0.co;2

Paxian, A., Sein, D., Panitz, H.-j., Warscher, M., Breil, M., Engel, T., et al. (2016). Bias reduction in decadal predictions of West African monsoon rainfall using regional climate models. *Journal of Geophysical Research: Atmospheres*, *121*(4), 1715–1735. https://doi.org/10.1002/2015jd024143

Pokam, W. M., Bain, C. L., Chadwick, R. S., Graham, R., Sonwa, D. J., & Kamga, F. M. (2014). Identification of processes driving low-level westerlies in West Equatorial Africa. *Journal of Climate*, *27*(11), 4245–4262. https://doi.org/10.1175/jcli-d-13-00490.1

Pokam, W. M., Djiotang, L. A. T., & Mkankam, F. K. (2012). Atmospheric water vapor transport and recycling in Equatorial Central Africa through NCEP/NCAR reanalysis data. *Climate Dynamics*, *38*(9–10), 1715–1729. https://doi.org/10.1007/s00382-011-1242-7

Pokam, W. M., Longandjo, G.-N. T., Moufouma-Okia, W., Bell, J.-P., James, R., Vondou, D. A., et al. (2018). Consequences of 1.5°C and 2°C global warming levels for temperature and precipitation changes over Central Africa. *Environmental Research Letters*, *13*(5), 055011. https://doi.org/10.1088/1748-9326/aab048

Ratnam, J. V., Morioka, Y., Behera, S. K., & Yamagata, T. (2015). A model study of regional air-sea interaction in the austral summer precipitation over southern Africa. *Journal of Geophysical Research: Atmospheres*, *120*(6), 2342–2357. https://doi.org/10.1002/2014jd022154

Roeckner, E., Arpe, K., Bengtsson, L., Christoph, M., Claussen, M., Dümenil, L., et al. (1996). *The Atmospheric General Circulation Model Echam-4: Model Description and Simulation of the Present Day Climate. Report No. 218*. Max-Planck-Institute for Meteorology.

Roeckner, E., Baeuml, G., Bonaventura, L., Brokopf, R., Esch, M., Giorgetta, M., et al. (2003). *The atmospheric general circulation model ECHAM 5. PART I: Model description Rep. 349*. MPI für Meteorol.

Rowell, D. P., Booth, B. B. B., Nicholson, S. E., & Good, P. (2015). Reconciling past and future rainfall trends over east Africa. *Journal of Climate*, *28*(24), 9768–9788. https://doi.org/10.1175/jcli-d-15-0140.1

Schneider, U., Hänsel, S., Finger, P., Rustemeier, E., & Ziese, M. (2022). GPCC full data monthly product version 2022 at 0.25°: Monthly land-surface precipitation from Rain-Gauges built on GTS-based and historical data [Dataset]. https://doi.org/10.5676/DWD_GPCC/FD_M_V2022_025

Seager, R., Naik, N., & Vecchi, G. A. (2010). Thermodynamic and dynamic mechanisms for large-scale changes in the hydrological cycle in response to global warming. *Journal of Climate*, *23*(17), 4651–4668. https://doi.org/10.1175/2010jcli3655.1

Sein, D. V., Koldunov, N. V., Pinto, J. G., & Cabos, W. (2014). Sensitivity of simulated regional Arctic climate to the choice of coupled model domain. *Tellus A: Dynamic Meteorology and Oceanography*, *66*(1), 23966. https://doi.org/10.3402/tellusa.v66.23966

Sein, D. V., Mikolajewicz, U., Gröger, M., Fast, I., Cabos, W., Pinto, J. G., et al. (2015). Regionally coupled atmosphere-ocean-sea ice-marine biogeochemistry model ROM: 1. Description and validation. *Journal of Advances in Modeling Earth Systems*, *7*(1), 268–304. https://doi.org/10.1002/2014ms000357

Seneviratne, S. I., Corti, T., Davin, E. L., Hirschi, M., Jaeger, E. B., Lehner, I., et al. (2010). Investigating soil moisture–climate interactions in a changing climate: A review. *Earth-Science Reviews*, *99*(3–4), 125–161. https://doi.org/10.1016/j.earscirev.2010.02.004

Sherwood, S. C., Bony, S., & Dufresne, J.-L. (2014). Spread in model climate sensitivity traced to atmospheric convective mixing. *Nature*, *505*(7481), 37–42. https://doi.org/10.1038/nature12829

Stachnik, J. P., & Schumacher, C. (2011). A comparison of the Hadley circulation in modern reanalyses. *Journal of Geophysical Research*, *116*(D22). https://doi.org/10.1029/2011jd016677

Tamoffo, A. T., Akinsanola, A. A., & Weber, T. (2023). Understanding the diversity of the West African monsoon system change projected by CORDEX-CORE regional climate models. *Climate Dynamics*, *61*(5–6), 2395–2419. https://doi.org/10.1007/s00382-023-06690-1

Tamoffo, A. T., Dosio, A., Vondou, D. A., & Sonkoué, D. (2020). Process-Based analysis of the added value of dynamical downscaling over Central Africa. *Geophysical Research Letters*, *47*(17). https://doi.org/10.1029/2020gl089702

Tamoffo, A. T., Dosio, A., Weber, T., & Vondou, D. A. (2023). Dynamic and thermodynamic contributions to late 21st century projected rainfall change in the Congo basin: Impact of a regional climate model's formulation. *Atmosphere*, *14*(12), 1808. https://doi.org/10.3390/atmos14121808

Tamoffo, A. T., Weber, T., Cabos, W., Monerie, P.-A., Cook, K. H., Sein, D. V., et al. (2024). West African monsoon system's responses to global ocean–regional atmosphere coupling. *Journal of Climate*, *37*(16), 4291–4312. https://doi.org/10.1175/jcli-d-23-0749.1

Tamoffo, A. T., Weber, T., Cabos, W., Sein, D. V., Dosio, A., Rechid, D., et al. (2024). Mechanisms of added value of a coupled global ocean-regional atmosphere climate model over Central Equatorial Africa. *Journal of Geophysical Research: Atmospheres*, *129*(3). https://doi.org/10.1029/2023jd039385

Thomas, N., & Nigam, S. (2018). Twentieth-Century climate change over Africa: Seasonal hydroclimate trends and Sahara desert expansion. *Journal of Climate*, *31*(9), 3349–3370. https://doi.org/10.1175/jcli-d-17-0187.1

van Vuuren, D. P., Edmonds, J., Kainuma, M., Riahi, K., Thomson, A., Hibbard, K., et al. (2011). The representative concentration pathways: An overview. *Climatic Change*, *109*(1–2), 5–31. https://doi.org/10.1007/s10584-011-0148-z

Vial, J., Bony, S., Dufresne, J., & Roehrig, R. (2016). Coupling between lower-tropospheric convective mixing and low-level clouds: Physical mechanisms and dependence on convection scheme. *Journal of Advances in Modeling Earth Systems*, *8*(4), 1892–1911. https://doi.org/10.1002/2016ms000740

Vizy, E. K., Manoj, H., & Cook, K. H. (2023). Is the climate of the Congo basin becoming less able to support a tropical forest ecosystem? *Journal of Climate*, *36*(23), 8171–8193. https://doi.org/10.1175/jcli-d-23-0275.1

Washington, R., James, R., Pearce, H., Pokam, W. M., & Moufouma-Okia, W. (2013). Congo Basin rainfall climatology: Can we believe the climate models? *Philosophical Transactions of the Royal Society B: Biological Sciences*, *368*(1625), 20120296. https://doi.org/10.1098/rstb.2012.0296

Weber, T., Cabos, W., Sein, D. V., & Jacob, D. (2022). Benefits of simulating precipitation characteristics over Africa with a regionally-coupled atmosphere–ocean model. *Climate Dynamics*, *60*(3–4), 1079–1102. https://doi.org/10.1007/s00382-022-06329-7

Whittleston, D., Nicholson, S. E., Schlosser, A., & Entekhabi, D. (2017). Climate models lack jet–rainfall coupling over West Africa. *Journal of Climate*, *30*(12), 4625–4632. https://doi.org/10.1175/jcli-d-16-0579.1

Zhang, C., Nolan, D. S., Thorncroft, C. D., & Nguyen, H. (2008). Shallow meridional circulations in the tropical atmosphere. *Journal of Climate*, *21*(14), 3453–3470. https://doi.org/10.1175/2007jcli1870.1

Zhou, T., Lu, J., Zhang, W., & Chen, Z. (2020). The sources of uncertainty in the projection of global land monsoon precipitation. *Geophysical Research Letters*, *47*(15). https://doi.org/10.1029/2020gl088415

Zou, L., & Zhou, T. (2016). A regional ocean–atmosphere coupled model developed for CORDEX East Asia: Assessment of Asian summer monsoon simulation. *Climate Dynamics*, *47*(12), 3627–3640. https://doi.org/10.1007/s00382-016-3032-8